Open and Hidden Charm Production at RHIC and LHC

R. Vogt

Nuclear Science Division, Lawrence Berkeley National Laboratory, Berkeley, CA 94720, USA

Physics Department, University of California, Davis, CA 95616, USA

Charm Hadrons

Open charm hadron production and decay can be detected both through lepton channels (semi-leptonic decays) and through pure hadronic channels (reconstruction of the D mass, momentum)

Table shows that measuring D mesons alone is not enough to get total $c\bar{c}$ cross section

C	Mass (GeV)	$c\tau$ (μm)	$B(C \to lX)$ (%)	$B(C \to$ Hadrons) (%)
$D^+(c\bar{d})$	1.869	315	17.2	$K^-\pi^+\pi^+$ (9.1)
$D^-(\bar{c}d)$	1.869	315	17.2	$K^+\pi^-\pi^-$ (9.1)
$D^0(c\bar{u})$	1.864	123.4	6.87	$K^-\pi^+$ (3.8)
$\overline{D^0}(\bar{c}u)$	1.864	123.4	6.87	$K^+\pi^-$ (3.8)
$D^{*\pm}$	2.010			$D^0\pi^\pm$ (67.7), $D^\pm\pi^0$ (30.7)
D^{*0}	2.007			$D^0\pi^0$ (61.9)
$D_s^+(c\bar{s})$	1.969	147	8	$K^+K^-\pi^+$ (4.4), $\pi^+\pi^+\pi^-$ (1.01)
$D_s^-(\bar{c}s)$	1.969	147	8	$K^+K^-\pi^-$ (4.4), $\pi^+\pi^-\pi^-$ (1.01)
$\Lambda_c^+(udc)$	2.285	59.9	4.5	ΛX (35), $pK^-\pi^+$ (2.8)
$\Sigma_c^{++}(uuc)$	2.452			$\Lambda_c^+\pi^+$ (100)
$\Sigma_c^+(udc)$	2.451			$\Lambda_c^+\pi^0$ (100)
$\Sigma_c^0(ddc)$	2.452			$\Lambda_c^+\pi^-$ (100)
$\Xi_c^+(usc)$	2.466	132		$\Sigma^+K^-\pi^+$ (1.18)
$\Xi_c^0(dsc)$	2.472	29		$\Xi^-\pi^+$ (seen)

Table 1: Ground state charm hadrons with their mass, decay length (when given) and branching ratios to leptons (when applicable) and some prominent decays to hadrons, preferably to only charged hadrons although such decays are not always available.

Experiments Measure Different Parts of Phase Space

Fixed Target Experiments

Longitudinal momentum fraction, x_F, is a useful observable, $x_F = 2p_L/\sqrt{S} = 2m_T \sinh y/\sqrt{S}$

Bubble chambers cover forward region, $x_F = 2p_L/\sqrt{S} = 2m_T \sinh y/\sqrt{S} > 0$

Beam dumps measuring either ν or μ

Proton beam dumped onto a dense target which suppresses π and K decays so that, when density is high enough, charm is only remaining lepton source

Extrapolate to infinite density to relate ν and μ flux to the $c\bar{c}$ cross section

Data preferentially at forward x_F, charm not directly reconstructed, momentum is more uncertain

ISR Collider Experiments

ISR experiments, at $\sqrt{S} = 53-63$ GeV, covered small part of phase space so results heavily dependent on extrapolation to full phase space

Some results come from dileptons, others from an electron trigger and a reconstructed charm hadron

Lepton channels ($e^{\pm}\mu^{\mp}$, e^+e^- and $\mu^+\mu^-$) give the most reasonable cross sections, $\sigma < 100$ μb

Hadron channel results assumed $pp \to \overline{D}\Lambda_c X$ characterized by $dN/dx_F \sim (1 - x_F)^n$

Used an electron, assumed to be from charm decay, opposite a reconstructed $\Lambda_c \to Kp\pi$ or $D \to K\pi\pi$

With x_F distribution assumed to go like $n \sim 0$ or $n \sim 3$, $\sigma \geq 500$ μb

Obtaining the Charm Cross Section from Data

To go from the D measurement (experiment) to the total charm cross section (theory calculation) we need to know how to extrapolate to full phase space and all charm hadrons

Accurate knowledge of decay branching ratios needed, some old measurements used significantly different branching ratios than those used today

Total number of "signal" charm counts determines the minimum bias cross section for the process

$$N_D = \sigma_D L t$$

where Lt is the luminosity over run time

Add up all the cross sections for measured D states, D^+, D^0 and their conjugates and correct for the unmeasured part, *e.g.* if coverage is $x_F > 0$, a calculated factor of 1.6 (pions) or 2 (protons) is needed to extrapolate to all x_F

$$\sigma_{c\bar{c}} = X \frac{\sigma_{D^+} + \sigma_{D^0} + \sigma_{D^-} + \sigma_{\overline{D^0}}}{2}$$

The factor of two is because the pair cross section is half the sum of the single hadron cross sections

Unmeasured part of total charm cross section represented by X

$X = 1.2$ (An Tai) $- 1.5$ (Frixione *et al.*) to account for D_s ($\approx 20\%$) and Λ_c ($\approx 30\%$) production (S. Aoki *et al.*, Prog. Theor. Phys. **87** (1992) 1305)

The A Dependence

Many experiments used nuclear targets to enhance statistics

A dependence of hard and soft processes are not the same — charm is a hard process

For hard processes, $\alpha \approx 1$, but nuclear effects tend to make $\alpha < 1$, albeit not by much

Total cross section A dependence parameterized as

$$\sigma_{pA} = \sigma_{pp} A^\alpha$$

Comes from integration over impact parameter, related to nuclear thickness function, $T_A = \int dz \rho_A(b, z)$,

$$\int d^2 b T_A(b) = A$$

Division by A gives the per nucleon cross section

α may drop with x_F, some indication of this from beam dump experiments

The A dependence of soft processes differs,

$$\alpha(x_F \sim 0) \approx 0.7$$
$$\alpha(x_F \sim 0.8) \approx 0.5$$

Soft behavior is seen for $p \to \pi, p, K, \Lambda$ with $\alpha = 0.72$ in minimum bias collisions

Some early experiments treated D production as a soft process

Charm is Hard Process, Calculable in Perturbative QCD

'Hard' processes have a large scale in the calculation that makes perturbative QCD applicable: high momentum transfer, μ^2, high mass, m, high transverse momentum, p_T

Asymptotic freedom assumed to calculate the interactions between two hadrons on the quark/gluon level but the confinement scale determines the probability of finding the interacting parton in the initial hadron

Factorization assumed between the perturbative hard part and the universal, nonperturbative parton distribution functions

The hadronic cross section in an AB collision where $AB = pp, pA$ or nucleus-nucleus is

$$\sigma_{AB}(S, m^2) = \sum_{i,j=q,\overline{q},g} \int_{4m_Q^2/s}^1 \frac{d\tau}{\tau} \int dx_1 \, dx_2 \, \delta(x_1 x_2 - \tau)$$
$$\times f_i^A(x_1, \mu_F^2) \, f_j^B(x_2, \mu_F^2) \, \widehat{\sigma}_{ij}(s, m^2, \mu_F^2, \mu_R^2)$$

f_i^A are the nonperturbative parton distributions, determined from fits to data, x_1 and x_2 are the fractional momentum of hadrons A and B carried by partons i and j, $\tau = s/S$

$\widehat{\sigma}_{ij}(s, m^2, \mu_F^2, \mu_R^2)$ is hard partonic cross section calculable in QCD in powers of α_s^{2+n}: leading order (LO), $n = 0$; next-to-leading order (NLO), $n = 1$ ...

Results depend strongly on quark mass, m, factorization scale, μ_F, in the parton densities and renormalization scale, μ_R, in α_s

Calculating the Total Cross Sections

Partonic total cross section only depends on quark mass m, not kinematic quantitites

To NLO

$$
\begin{aligned}
\hat{\sigma}_{ij}(s, m, \mu_F^2, \mu_R^2) &= \frac{\alpha_s^2(\mu_R^2)}{m^2} \Big\{ f_{ij}^{(0,0)}(\rho) \\
&+ 4\pi\alpha_s(\mu_R^2)\left[f_{ij}^{(1,0)}(\rho) + f_{ij}^{(1,1)}(\rho)\ln(\mu_F^2/m^2) \right] + \mathcal{O}(\alpha_s^2) \Big\}
\end{aligned}
$$

$\rho = 4m^2/s$, s is partonic center of mass energy squared

μ_F is factorization scale, separates hard part from nonperturbative part

μ_R is renormalization scale, scale at which strong coupling constant α_s is evaluated

$\mu_F = \mu_R$ in evaluations of parton densities

$f_{ij}^{(a,b)}$ are dimensionless, μ-independent scaling functions, $a = 0$, $b = 0$ and $ij = q\bar{q}$, gg for LO, $a = 1$, $b = 0, 1$ and $ij = q\bar{q}$, gg and qg, $\bar{q}g$ for NLO

$f_{ij}^{(0,0)}$ are always positive, $f_{ij}^{(1,b)}$ can be negative also

Note that if $\mu_F^2 = m^2$, $f_{ij}^{(1,1)}$ does not contribute

Scaling Functions to NLO

Near threshold, $\sqrt{s}/2m \to 1$, Born contribution is large but dies away for $\sqrt{s}/2m \to \infty$

At large $\sqrt{s}/2m$, gg channel is dominant, then qg

Given high energy behavior of the scaling functions, large changes in the energy dependence of hadronic cross section are difficult to achieve
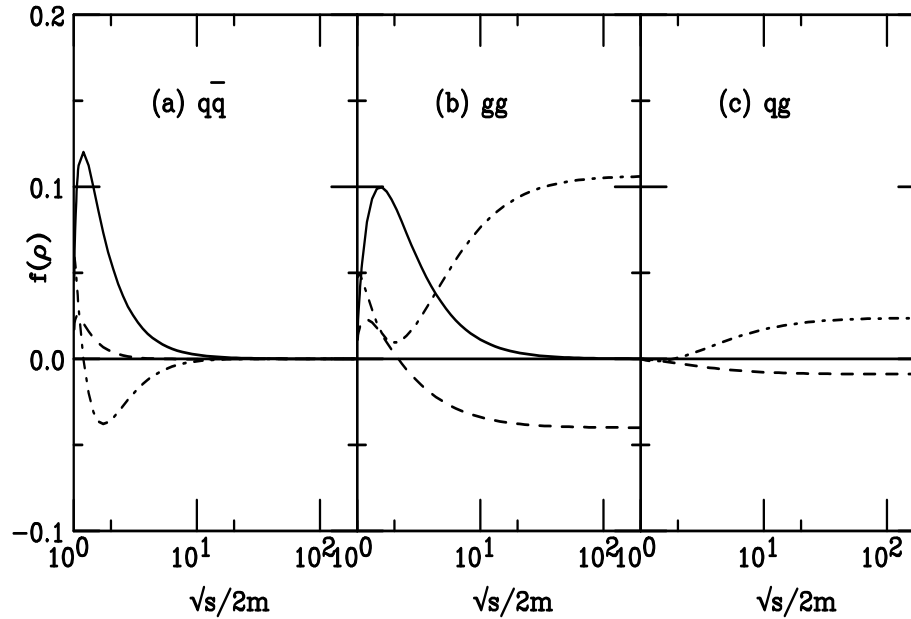
.

Figure 1: Scaling functions needed to calculate the total partonic $Q\overline{Q}$ cross section. The solid curves are the Born results, $f_{ij}^{(0,0)}$, the dashed and dot-dashed curves are NLO contributions, $f_{ij}^{(1,1)}$ and $f_{ij}^{(1,0)}$ respectively.

Fixing NLO Parameters m and μ^2 to All Data

Difficult to obtain a large calculated $c\bar{c}$ cross section with $\mu_F^2 = \mu_R^2$, as in parton density fits

Data favors lower masses – lowest mass used here is 1.2 GeV but much lower masses than allowed in pQCD needed to agree with largest cross sections
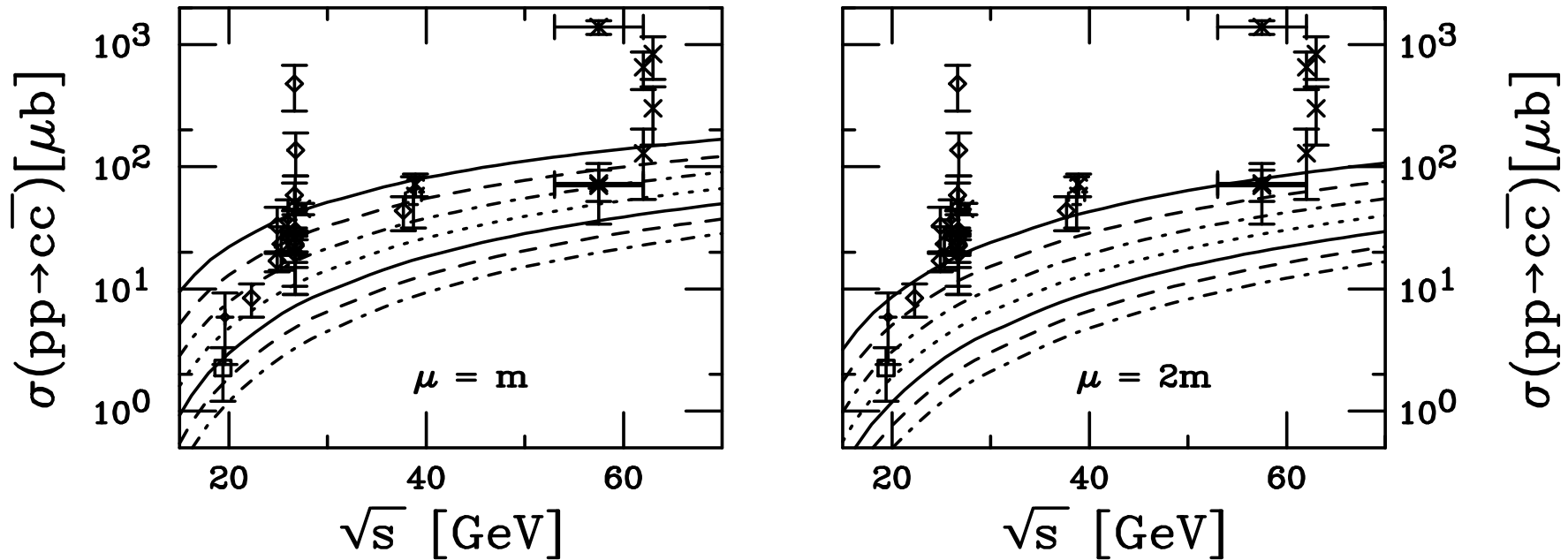
Figure 2: Total $c\bar{c}$ cross sections in pp and pA interactions up to ISR energies as a function of the charm quark mass. All calculations are fully NLO using the MRST HO (central gluon) parton densities. The left-hand plot shows the results with the renormalization and factorization scales equal to m while in the right-hand plot the scale is set to $2m$. From top to bottom the curves are $m = 1.2$, 1.3, 1.4, 1.5, 1.6, 1.7, and 1.8 GeV.

Agreement Found for Several Cases
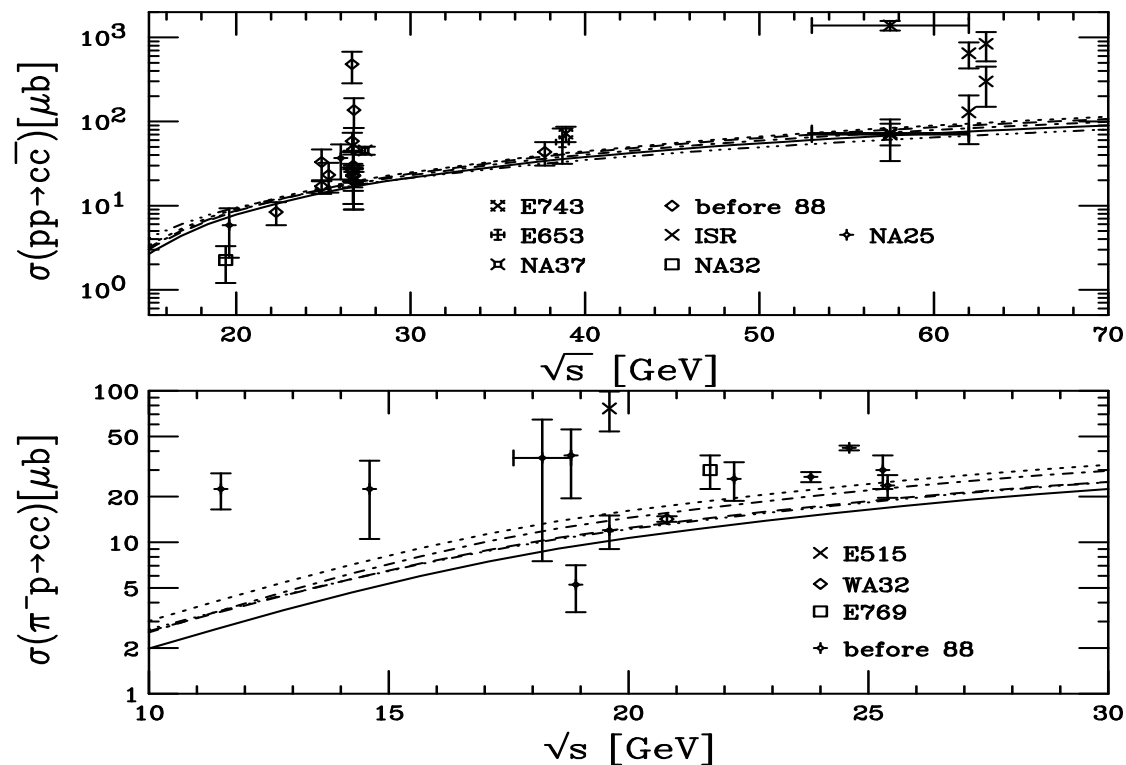
Figure 3: Total $c\bar{c}$ cross sections in pp and $\pi^- p$ interactions compared to data. All calculations are fully NLO. The curves are: MRST HO (central gluon) with $\mu = m = 1.4$ GeV (solid) and $\mu = 2m = 2.4$ GeV (dashed); CTEQ 5M with $\mu = m = 1.4$ GeV (dot-dashed) and $\mu = 2m = 2.4$ GeV (dotted); and GRV98 HO with $\mu = m = 1.3$ GeV.

Extrapolation to Higher Energies

Only two curves remain, MRST HO with $m = 1.2$ GeV, $\mu^2 = 4m^2$ and GRV98 HO with $m = 1.3$ GeV, $\mu^2 = m^2$

We have kept only the most recent measurements, including the PHENIX $\sqrt{S} = 130$ GeV result from Au+Au

The current STAR point lies well above these results
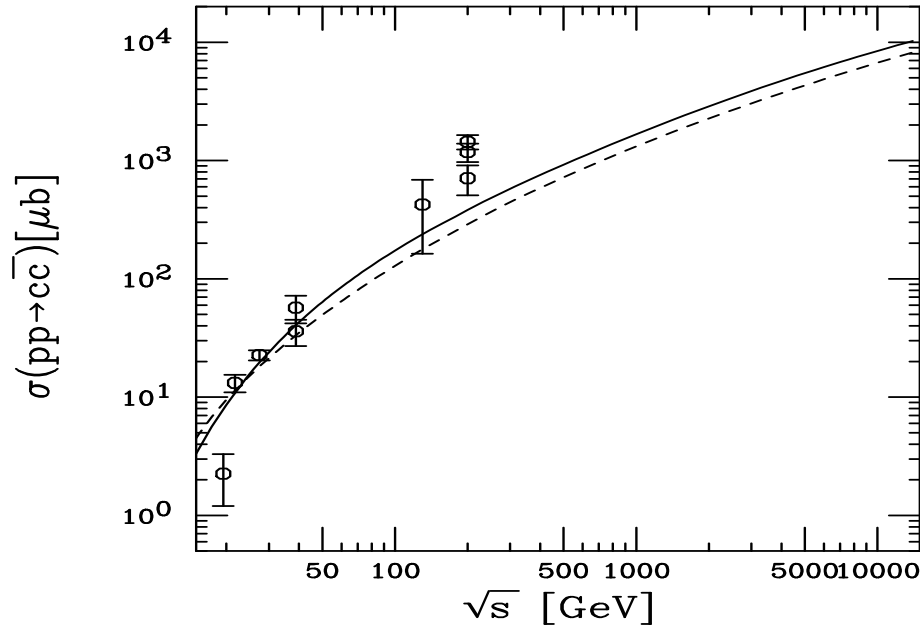
Figure 4: Total $c\bar{c}$ cross sections in pp interactions up to 14 TeV. All calculations are fully NLO. The curves are MRST HO (central gluon) with $m = 1.2$ GeV and $\mu^2 = 4m^2$ (dashed) and GRV98 HO with $m = 1.3$ GeV and $\mu^2 = m^2$.

Can σ Be Increased? Varying μ_F^2 and μ_R^2

Choose μ_F and μ_R separately so that $\mu_R^2 \leq \mu_F^2$

Going to smaller μ_F does not help, would go below minimum μ^2 for the parton density set

Reducing μ_R^2 increases α_s since $\mu_R^2/\Lambda_{\rm QCD}^2$ gets smaller

Changing μ_F and μ_R does not change slope or improve agreement
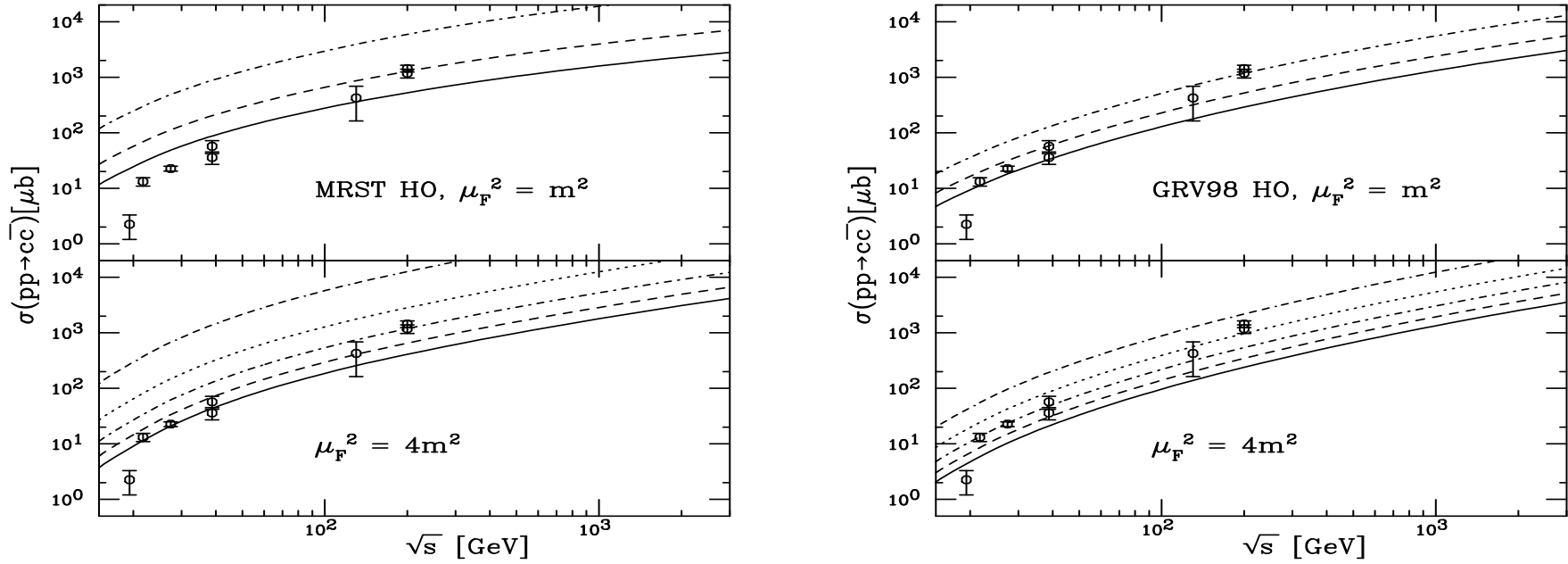
Figure 5: Total $pp \rightarrow c\bar{c}$ cross sections calculated for (left-hand side) the MRST HO densities with $m = 1.2$ GeV and (right-hand side) the GRV98 HO densities with $\mu_F^2 = m^2$ (upper) and $\mu_F^2 = 4m^2$ (lower). In the upper plot the values of μ_R^2 are m^2 (solid), $m^2/2$ (dashed) and $m^2/4$ (dot dashed). In the lower plot, $\mu_R^2 = 4m^2$ (solid), $2m^2$ (dashed), m^2 (dot-dashed), $m^2/2$ (dotted) and $m^2/4$ (dot-dash-dash-dashed).

K Factors Smallest when $\mu_F^2 = \mu_R^2$

K factors ($\sigma_{\mathrm{NLO}}/\sigma_{\mathrm{LO}}$) measure the stability and convergence of perturbative expansion

K factor larger for MRST HO when $\mu_F^2 = m^2$, close to minimum μ^2 for these densities, GRV98 HO densities have $\mu_F^2 = m^2 > \mu_{\min}^2$

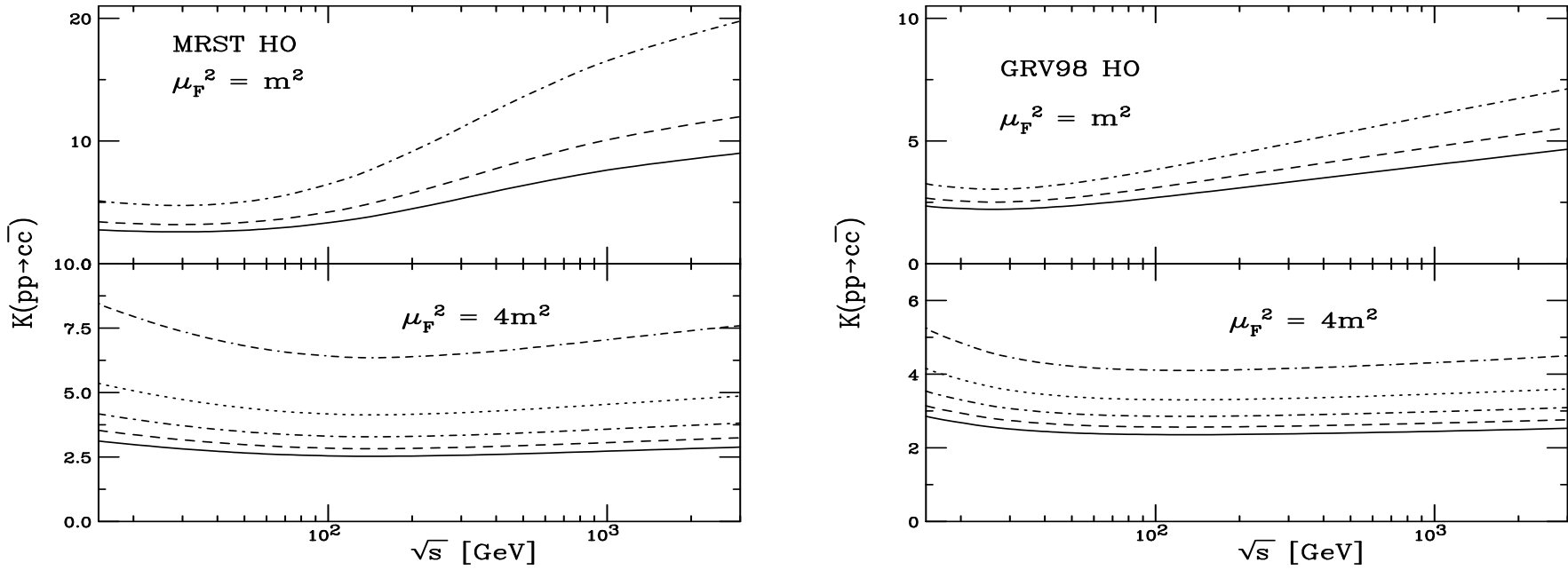K factors are large, $K > 2$, so next order corrections remain important

Figure 6: The $c\bar{c}$ K factors in pp interactions calculated using (left-hand side) the MRST HO densities and $m = 1.2$ GeV and (right-hand side) the GRV98 HO densities and $m = 1.3$ GeV with $\mu_F^2 = m^2$ (upper) and $\mu_F^2 = 4m^2$ (lower). In the upper plot the values of μ_R^2 are m^2 (solid), $m^2/2$ (dashed) and $m^2/4$ (dot dashed). In the lower plot, $\mu_R^2 = 4m^2$ (solid), $2m^2$ (dashed), m^2 (dot-dashed), $m^2/2$ (dotted) and $m^2/4$ (dot-dash-dash-dashed).

Can the NLO Cross Section Be Calculated Another Way?

Inclusive charm hadroproduction cross section

$$d\sigma_{pp\to c\bar{c}X}(\sqrt{s}, m, \mu_R^2, \mu_F^2) \sum_{i,j=q,\bar{q},g} f_i(x_1, \mu_F^2) \otimes f_j(x_2, \mu_F^2) \otimes d\hat{\sigma}_{ij\to c\bar{c}\{k\}}(\alpha_s(\mu_R^2), \mu_F^2, m, x_1, x_2)$$

$k = 0$ at LO and 0, q, $\bar{q}$ or g at NLO

NLO cross section can be calculated in two ways:

- "standard NLO" — NLO PDFs and two-loop α_s at each order

$$
\begin{aligned}
d\sigma_{\text{NLO}}^{\text{std}} &= \sum_{i,j=q,\bar{q},g} f_i^{\text{NLO}}(x_1, \mu_F^2) \otimes f_j^{\text{NLO}}(x_2, \mu_F^2) \otimes d\hat{\sigma}_{ij\to c\bar{c}}^{\text{LO}}(\alpha_s^{\text{2L}}(\mu_R^2), x_1, x_2) \\
&+ \sum_{i,j=q,\bar{q},g} f_i^{\text{NLO}}(x_1, \mu_F^2) \otimes f_j^{\text{NLO}}(x_2, \mu_F^2) \otimes \sum_{k=0,q,\bar{q},g} d\hat{\sigma}_{ij\to c\bar{c}k}^{\text{NLO}}(\alpha_s^{\text{2L}}(\mu_R^2), \mu_F^2, x_1, x_2) \\
&\equiv d\sigma_{\text{LO}}^{\text{2L}} + d\sigma_{\mathcal{O}(\alpha_s^3)}
\end{aligned}
$$

- "alternative NLO" — LO PDFs and one-loop α_s for LO part, NLO PDFs and two-loop α_s for NLO contribution

$$
\begin{aligned}
d\sigma_{\text{NLO}}^{\text{alt}} &= \sum_{i,j=q,\bar{q},g} f_i^{\text{LO}}(x_1, \mu_F^2) \otimes f_j^{\text{LO}}(x_2, \mu_F^2) \otimes d\hat{\sigma}_{ij\to c\bar{c}}^{\text{LO}}(\alpha_s^{\text{1L}}(\mu_R^2), x_1, x_2) \\
&+ \sum_{i,j=q,\bar{q},g} f_i^{\text{NLO}}(x_1, \mu_F^2) \otimes f_j^{\text{NLO}}(x_2, \mu_F^2) \otimes \sum_{k=0,q,\bar{q},g} d\hat{\sigma}_{ij\to c\bar{c}k}^{\text{NLO}}(\alpha_s^{\text{2L}}(\mu_R^2), \mu_F^2, x_1, x_2) \\
&\equiv d\sigma_{\text{LO}}^{\text{1L}} + d\sigma_{\mathcal{O}(\alpha_s^3)}
\end{aligned}
$$

Alternative NLO Cross Section Larger at High $\sqrt{S}$

$\sigma_{\rm NLO}^{\rm alt} > \sigma_{\rm NLO}^{\rm std}$ at large $\sqrt{S}$ because NLO gluon distributions can become small or negative at low x

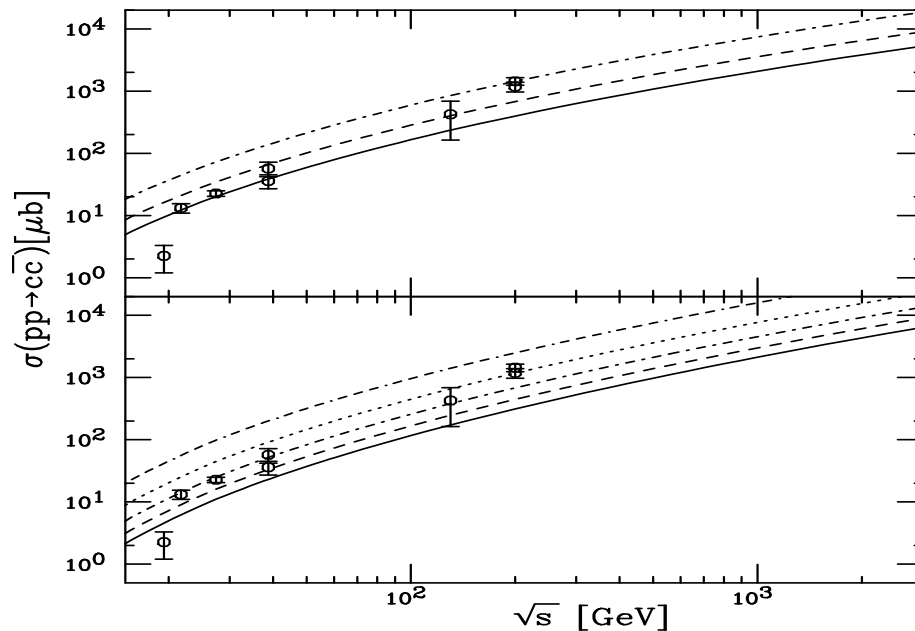Effect is not large enough to make a significant change in $\sqrt{S}$ dependence at RHIC

Figure 7: Total $pp \to c\bar{c}$ cross sections calculated using the alternative NLO result. The cross sections are obtained for the GRV98 HO densities with $m = 1.3$ GeV and $\mu_F^2 = m^2$ (upper) and $\mu_F^2 = 4m^2$ (lower). In the upper plot the values of μ_R^2 are m^2 (solid), $m^2/2$ (dashed) and $m^2/4$ (dot dashed). In the lower plot, $\mu_R^2 = 4m^2$ (solid), $2m^2$ (dashed), m^2 (dot-dashed), $m^2/2$ (dotted) and $m^2/4$ (dot-dash-dash-dashed).

Using $\sigma_{\text{NLO}}^{\text{alt}}$ Reduces K

Energy dependence of K factor defined as $\sigma_{\text{NLO}}^{\text{alt}}/\sigma_{\text{LO}}^{\text{1L}}$ is reduced, especially at high $\sqrt{S}$

At fixed target energies, $\sigma_{\text{NLO}}^{\text{alt}}$ and $\sigma_{\text{NLO}}^{\text{std}}$ differ by only the values of one- and two-loop α_s ($\alpha_s^{\text{1L}} > \alpha_s^{\text{2L}}$) since LO and NLO gluon densities are similar at large x
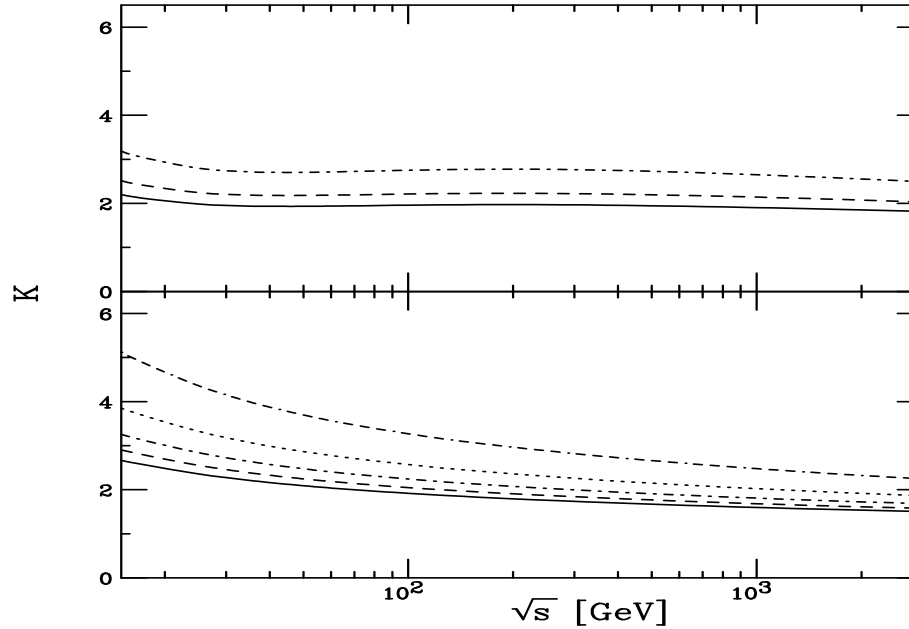

Figure 8: The $c\bar{c}$ K factors in pp interactions calculated using the alternative NLO cross sections with the GRV98 HO densities, $m = 1.3$ GeV and $\mu_F^2 = m^2$ (upper) and $\mu_F^2 = 4m^2$ (lower). In the upper plot the values of μ_R^2 are m^2 (solid), $m^2/2$ (dashed) and $m^2/4$ (dot dashed). In the lower plot, $\mu_R^2 = 4m^2$ (solid), $2m^2$ (dashed), m^2 (dot-dashed), $m^2/2$ (dotted) and $m^2/4$ (dot-dash-dash-dashed).

From Total Cross Sections to Distributions

In total cross section, the quark mass is the only relevant scale

When considering kinematical observables like x_F or p_T, the momentum scale is also relevant so that, instead of $\mu^2 \propto m^2$, one usually uses $\mu^2 \propto m_T^2$

Other important considerations for distributions: fragmentation and intrinsic k_T

Fragmentation assumed to be universal, like parton densities, so the parameterizations of e^+e^- data (*e.g.* Peterson function) should work in hadroproduction

Effect of intrinsic transverse momentum broadening decreases with energy

Bare Quark p_T Distributions as a Function of m and μ

Differences largest at low p_T, determines total cross section
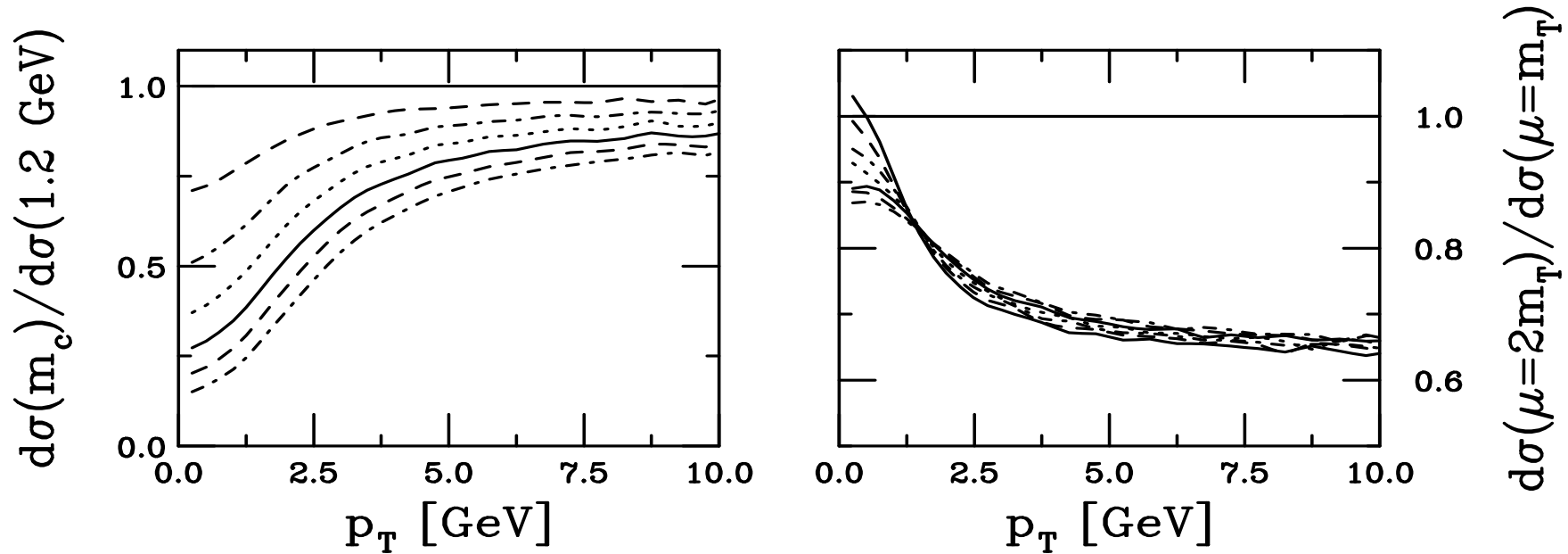
Distributions become similar at high p_T
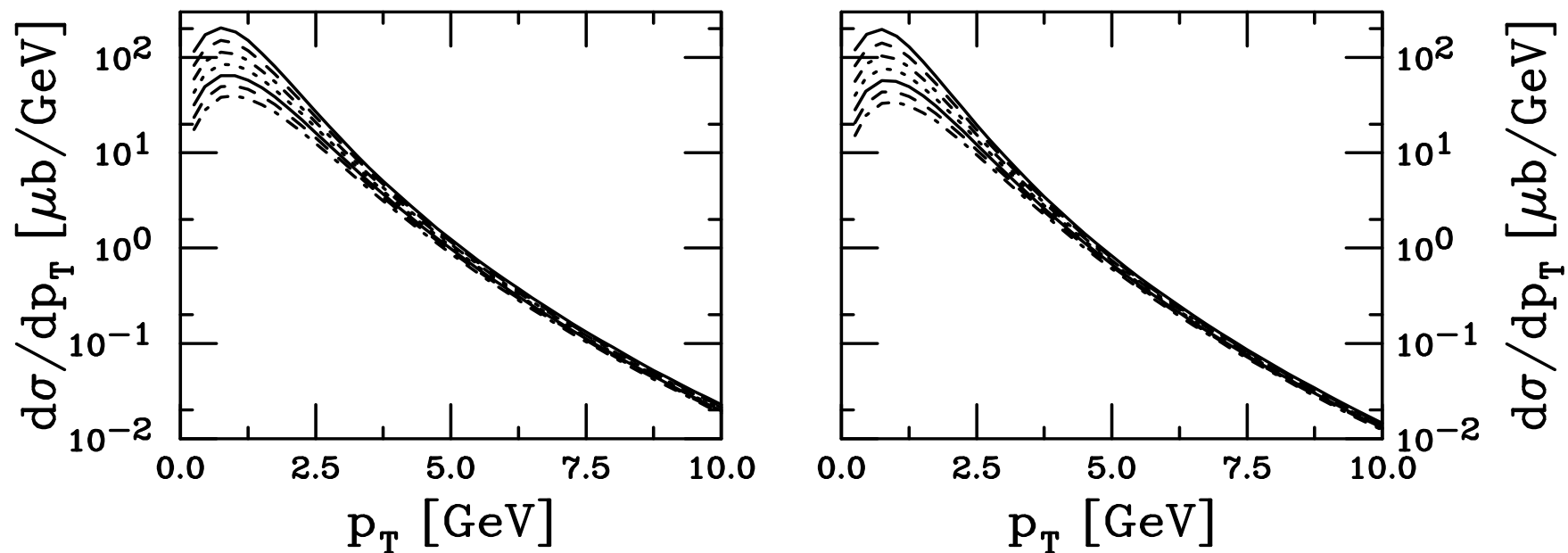
Figure 9: The NLO charm quark p_T distributions in pp interactions at $\sqrt{S} = 200$ GeV as a function of the charm quark mass calculated with the GRV98 HO parton densities, integrated over all rapidity. The left-hand plot shows the results with the renormalization and factorization scales equal to m_T while in the right-hand plot the scale is set to $2m_T$. From top to bottom the curves are $m = 1.2$, 1.3, 1.4, 1.5, 1.6, 1.7, and 1.8 GeV.

Average Bare Quark p_T as a Function of m and μ

Average p_T increases with m

Average p_T decreases with μ

	$\mu = m_T$	$\mu = 2m_T$
m_c (GeV)	$\langle p_T \rangle$ (GeV)	$\langle p_T \rangle$ (GeV)
1.2	1.17	1.08
1.3	1.23	1.15
1.4	1.29	1.21
1.5	1.35	1.28
1.6	1.41	1.35
1.7	1.48	1.41
1.8	1.54	1.48

Table 2: Average charm quark p_T for various mass and scale combinations.

Parameter Variation of p_T Distributions

Ratios of cross sections relative to $m = 1.2$ GeV shows largest difference at low p_T, similar results for $\mu = m_T$ and $2m_T$

Ratio of cross sections with $\mu = 2m_T$ relative to those with $\mu = m_T$ at the same mass value are almost independent of mass

Figure 10: The ratios NLO charm quark p_T distributions in pp interactions at $\sqrt{S} = 200$ GeV as a function of the charm quark mass calculated with the GRV98 HO parton densities. The left-hand plot shows the ratio of the p_T distributions to that with $m = 1.2$ GeV while the right-hand plot shows the ratio of the result with $\mu = 2m_T$ relative to $\mu = m_T$ for each value of m. From top to bottom the curves are $m = 1.2, 1.3, 1.4, 1.5, 1.6, 1.7,$ and 1.8 GeV.

Adding Fragmentation and Intrinsic k_T

Double differential cross sections

$$s^2 \frac{d^2\sigma_{pp}(s,t,u)}{dtdu} = \sum_{i,j=q,\overline{q},g} \int_{x_1^-}^1 \frac{dx_1}{x_1} \int_{x_2^-}^1 \frac{dx_2}{x_2} f_i^p(x_1,\mu^2) f_j^p(x_2,\mu^2) \mathcal{J}_K(\hat{s},\hat{t},\hat{u}) \hat{s}^2 \frac{d^2\hat{\sigma}_{ij}(\hat{s},\hat{t},\hat{u})}{d\hat{t}d\hat{u}}$$

$f_i^p = F_i^p/x$ is parton density, $\mathcal{J}_K$ is a kinematics-dependent Jacobian

Intrinsic transverse momentum and fragmentation are needed to smear the pair p_T and ϕ distributions as measured for $D\overline{D}$ correlations (Peterson fragmentation and $k_T^2 = 1$ GeV^2 cancel each other in low $\sqrt{S}$ single D p_T distributions)

Adds the following extra integrations:

$$\int dz_3 dz_4 d^2 k_{T1} d^2 k_{T2} \frac{D_{H/Q}(z_3,\mu^2)}{z_3} \frac{D_{\overline{H}/\overline{Q}}(z_4,\mu^2)}{z_4} g_p(k_{T1}) g_p(k_{T2})$$

Fragmentation function a la Peterson

$$D_{H/Q}(z) = \frac{N}{z(1 - 1/z - \epsilon_Q/(1-z))^2}$$

$\epsilon_Q = 0.06$ for charm, 0.006 for bottom, normalized so that $\Sigma_H \int D_{H/Q}(z)dz = 1$ for all H hadrons from Q

Gaussian k_T smearing, $\langle k_T^2 \rangle_p = 1$ GeV^2 for pp, broadened for pA and AA, NLO code adds in final state

$$g_p(k_T) = \frac{1}{\pi \langle k_T^2 \rangle_p} \exp(-k_T^2/\langle k_T^2 \rangle_p)$$

Bare Quark Distribution Works Better for x_F

$x_F = 2p_L/\sqrt{S} = 2m_T \sinh y/\sqrt{S}$ distributions integrated over p_T, average goes into m_T in x_F

$pp \to DX$ at 400 GeV, fixed target shown here

Bare distribution (delta function) works better than the Peterson function (dashed curve) which falls below data
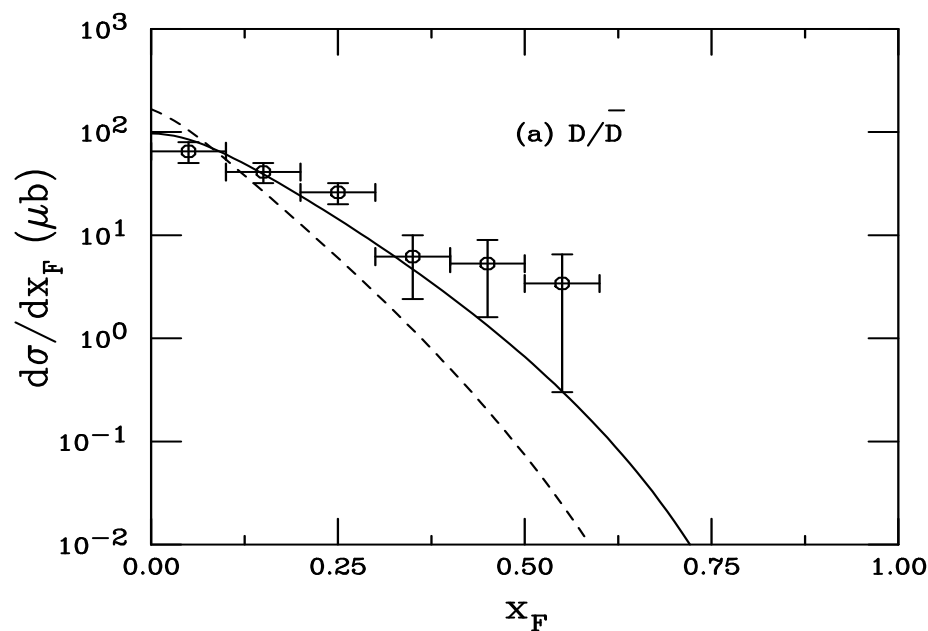

Figure 11: Comparison of calculations with data from 400 GeV pp interactions. The dashed curve uses the Peterson function while the solid curve is a delta function. The data are from M. Aguilar-Benitez *et al.*, Phys. Lett. **B189**, 476 (1987), the calculations from R.V. *et al.*, Nucl. Phys. **B383**, 643 (1992).

Cancelation of Fragmentation and k_T at $\sqrt{S} = 16$ GeV

Bare charm (solid) and Peterson fragmentation with $\langle k_T^2 \rangle = 1$ GeV^2 (dotted) on top of each other

Broadening alone, $\langle k_T^2 \rangle = 1$ GeV^2, widens p_T distribution

Peterson fragmentation alone (dot-dashed) below bare

Large $\langle k_T^2 \rangle$ (dot-dot-dot-dashed) in between
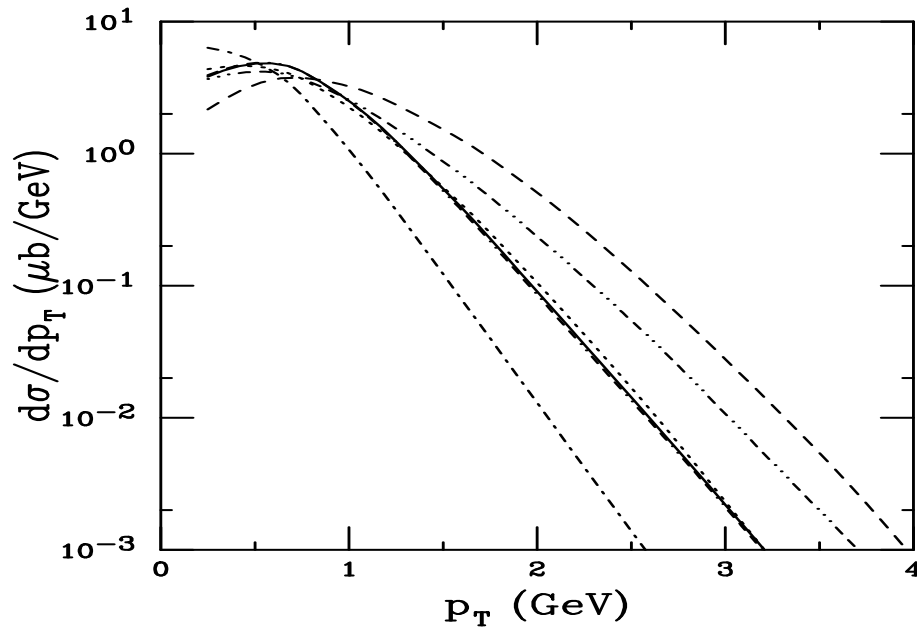
Figure 12: For a fixed-target experiment with $p_{\rm lab} = 158$ GeV, we compare the NLO p_T distributions including fragmentation and intrinsic k_T. The solid curves shows the bare distribution, the dashed includes $\langle k_T^2 \rangle = 1$ GeV^2 but no fragmentation, the dot-dashed is Peterson fragmentation alone, the dotted and dot-dot-dot-dashed include both Peterson fragmentation and broadening with $\langle k_T^2 \rangle = 1$ and 1.7 GeV^2 respectively.

No Cancelation at RHIC

$\langle k_T^2 \rangle = 1$ GeV^2 alone (dashed) is now a small effect since $\langle p_T \rangle$ is much larger than at fixed-target energies

Peterson fragmentation alone (dot-dashed) below bare distribution, going to higher $\langle k_T^2 \rangle$ does not help, 1.7 GeV^2 is largest shown, even 4 GeV^2 does not bring the result closer to the bare distribution
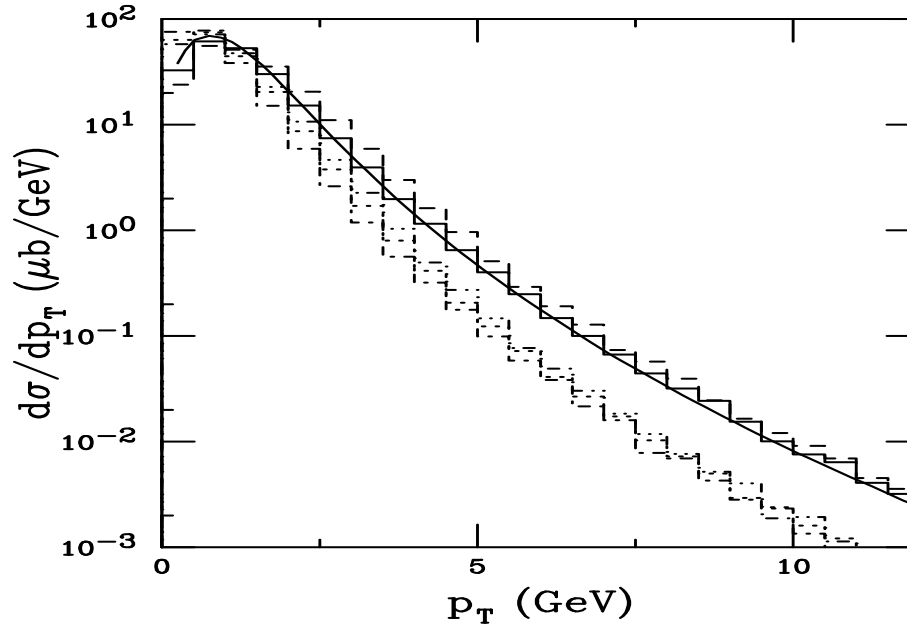
Figure 13: We compare the NLO p_T distributions including fragmentation and intrinsic k_T at $\sqrt{S_{NN}} = 200$ GeV. The solid curve and solid histogram shows the bare distribution calculated both as a single inclusive distribution and in exclusive pair production, the dashed includes $\langle k_T^2 \rangle = 1$ GeV^2 but no fragmentation, the dot-dashed is Peterson fragmentation alone, the dotted and dot-dot-dot-dashed include both Peterson fragmentation and broadening with $\langle k_T^2 \rangle = 1$ and 1.7 GeV^2 respectively.

Dependence of p_T Distributions on Parton Densities

Both MRST HO and GRV98 HO parton densities agree well with lower energy data for total cross section

Preliminary STAR reconstructed D and D^* data agree with shape of NLO bare quark p_T distribution

.
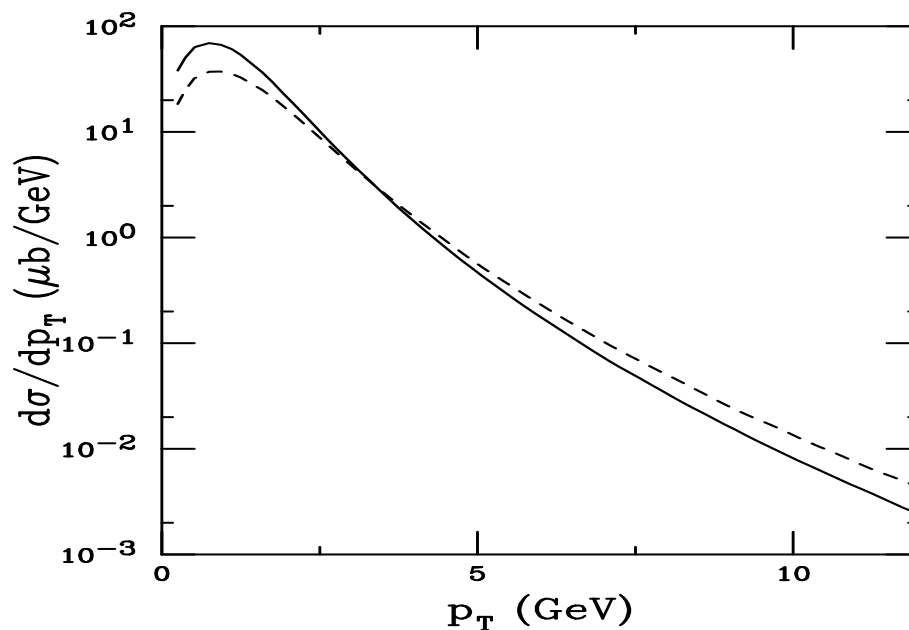
Figure 14: The NLO bare charm quark distributions at $\sqrt{S} = 200$ GeV. The dashed curve shows the NLO calculation with the GRV98 HO parton densites, $m = 1.3$ GeV and $\mu = m_T$ while the solid curve is the result with MRST HO parton densities, $m = 1.2$ GeV and $\mu = 2m_T$.

Comparison With STAR Data

Some of the p_T distributions shown previously compared to STAR data

Good agreement with shape but not normalization
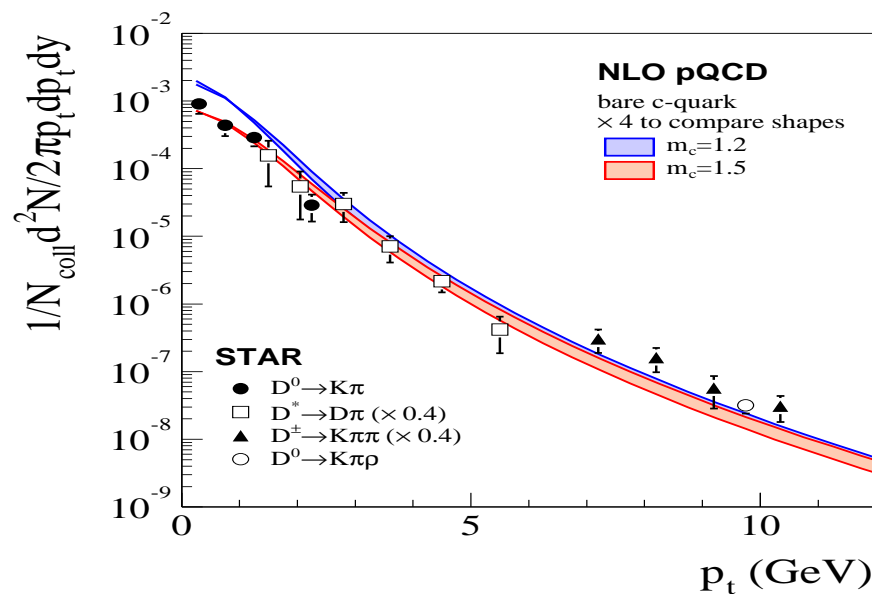
Figure 15: The STAR D meson data is compared to NLO bare charm calculations. The curves, calculated with the GRV98 HO parton densites, show a range of mass and scale values. They are scaled by a factor of 4 to agree with the normalization of the data. [Thanks to Marco van Leeuwen for the plot, see his talk for more details.]

Other Models of Charm p_T Distributions

FONLL scheme (Cacciari and Nason):

Designed to cure logs of p_T/m for $p_T \gg m$

Adds subset of NLL exponents with equivalent NLO terms subtracted out

Gives lower total cross section, falls faster than preliminary data at high p_T

Unintegrated parton densities (Kharzeev and Tuchin):

Uses transverse momentum unintegrated gluon distributions and matrix elements (Collins) to calculate small x corrections

Similar to NLO at large p_T but overestimates low p_T contribution relative to data
Unintegrated gluon densities very uncertain

Charm Not Produced at Very Low x at RHIC

Compare μ^2 and x at several values of charm quark rapidity when rapidity of unobserved c (or $\bar{c}$) integrated away, $m = 1.2$ GeV, $\mu^2 = 4m_T^2$

$x_2 = (2m_T/\sqrt{S})(\exp(-y) + \exp(-y_2)) \geq 0.01$ at LO, not symmetric around $y = 0$

Higher energies (and forward rapidities) needed to reach the low x regime, see talk of A. Dainese for some futher discussion   .
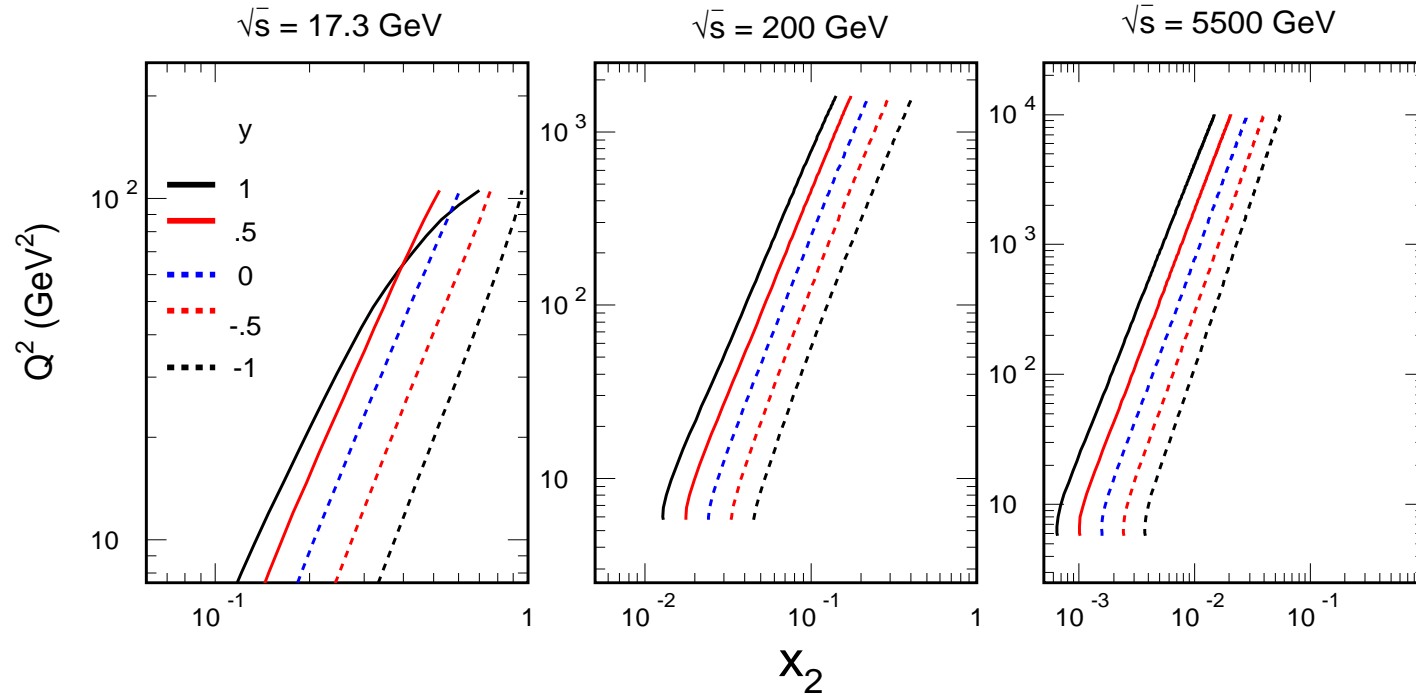
Figure 16: Curves of Q^2 as a function of x_2 for $y = 1, 0.5, 0, -0.5$ and -1 when the rapidity of the unobserved quark is integrated away. (With N. Xu and L. Grandchamp.)

Comparison of STAR and CDF x_T Distributions

To better compare RHIC and Tevatron results, the $x_T = 2p_T/\sqrt{S}$ distributions are constructed for both charm and charged hadron distributions

CDF and STAR D slopes are similar for STAR $p_T > 3$ GeV

CDF x_T distributions shifted to smaller x_T by $\sqrt{S_{\text{STAR}}}/\sqrt{S_{\text{CDF}}} \sim 0.1$
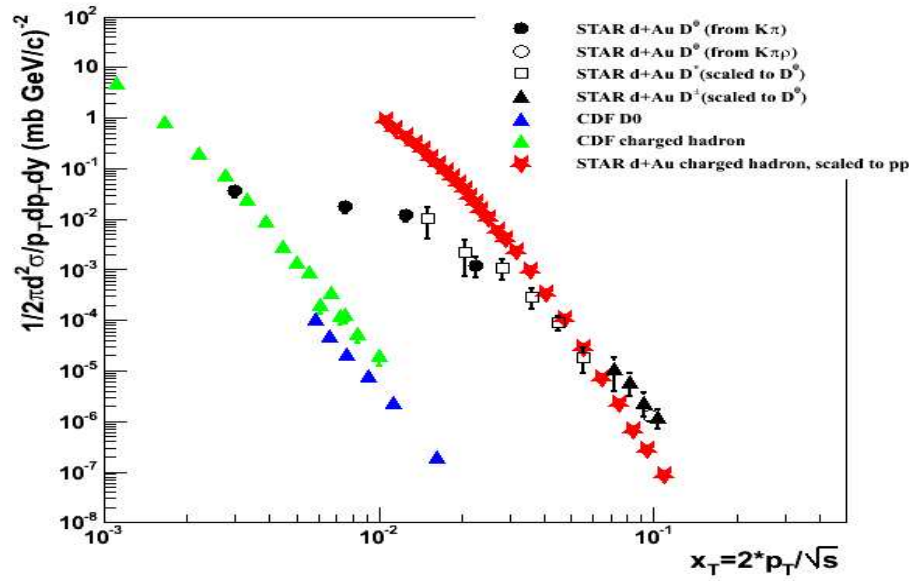
Figure 17: Comparison of STAR ($\sqrt{S_{NN}} = 200$ GeV) and CDF ($\sqrt{S} = 1960$ GeV) x_T distributions for D mesons and charged hadrons. [Plot courtesy of An Tai (STAR).]

CDF Data Agrees with NLO Bare Charm Distribution

CDF data shown are sum of D^+ and D^0 (and conjugate) distributions, error bars are convolution of statistical and systematic errors

No rescaling is needed to reach agreement with the data
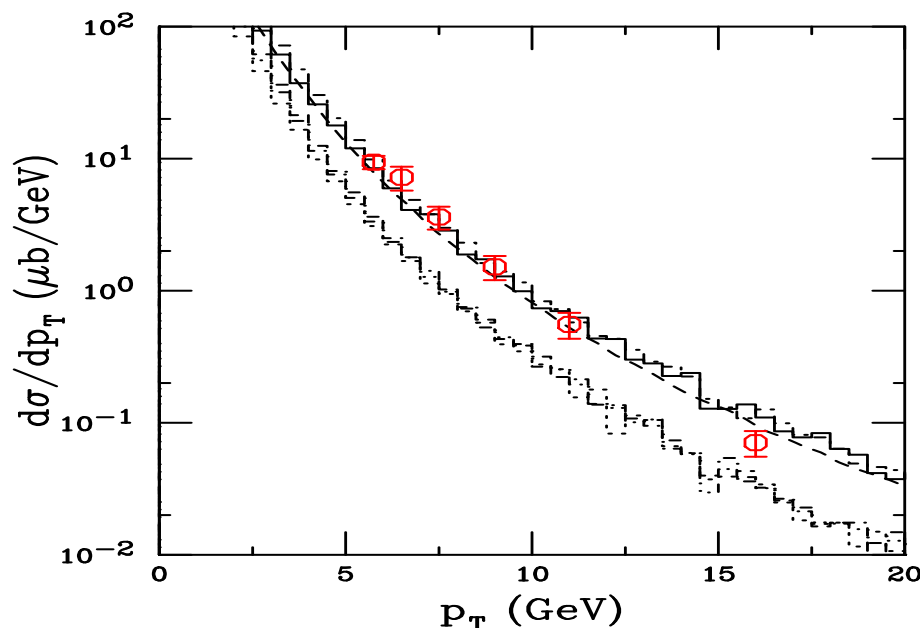
Figure 18: We compare the NLO p_T distributions including fragmentation and intrinsic k_T at $\sqrt{S_{NN}} = 1.96$ TeV compared to the CDF data. The upper solid histogram and curve shows the bare distribution, the dashed includes $\langle k_T^2 \rangle = 1$ GeV^2 but no fragmentation, the dot-dashed is Peterson fragmentation alone, the dotted and lower solid include both Peterson fragmentation and broadening with $\langle k_T^2 \rangle = 1$ and 1.7 GeV^2 respectively.

Why Doesn't Fragmentation Agree With Data?

- Effect of intrinsic k_T weak at high energy where $\langle p_T \rangle$ of heavy quark is larger than at fixed-target energies

- Peterson function is old, assumes charm quark loses on average 30% of its momentum, may be newer parameterizations which reduce momentum loss

- Violation of factorization? Either fragmentation may not be universal or we just don't understand it well enough yet

- What about coalescence? In hadronic hard scatterings, initial hadrons break up, freeing partons comoving with the charm quark to coalesce into hadron with little momentum loss (suggested by R.V., Brodsky and Hoyer, 92)

LHC Charm Distributions

Charm quark p_T distributions reveal increasing $\langle p_T \rangle$ with $\sqrt{S}$

p_T distributions harden at higher p_T as $\sqrt{S}$ increases
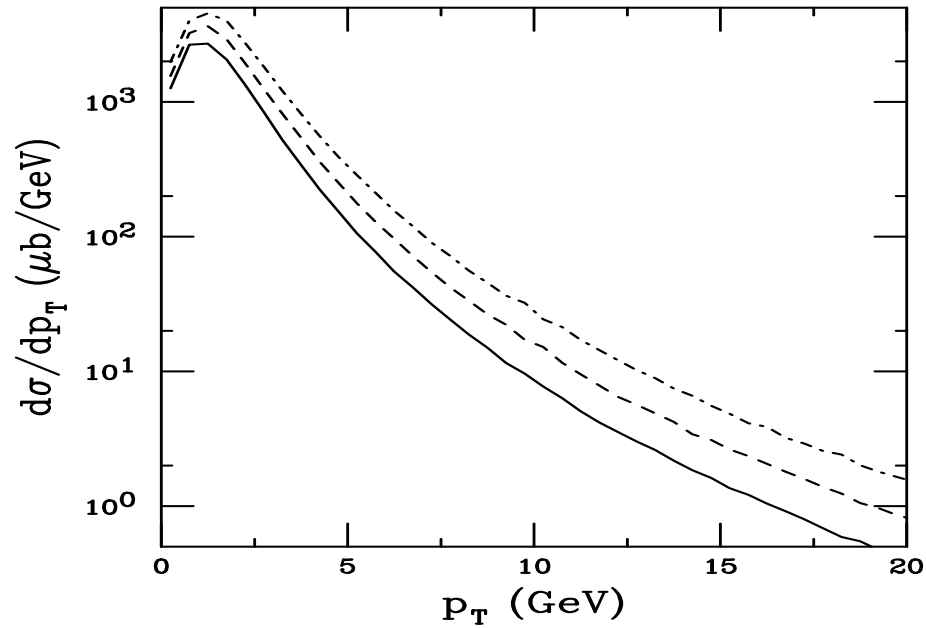
Figure 19: The NLO bare charm inclusive p_T distributions at $\sqrt{S} = 5.5$ (solid), 8.8 (dashed) and 14 (dot-dashed) TeV.

Influence on J/ψ of Large $\sigma_{c\bar{c}}$

Regeneration of J/ψ possible when more than 1 $c\bar{c}$ pair produced per event

$\sigma_{c\bar{c}} \approx 0.35$ mb from pQCD, about 8 $c\bar{c}$ pairs/event

Preliminary STAR cross section, $1.1 - 1.4$ mb, $26 - 33$ $c\bar{c}$/event, increasing J/ψ yield per collision
Increase inconsistent with PHENIX Au+Au data, PHENIX pp result more consistent with pQCD
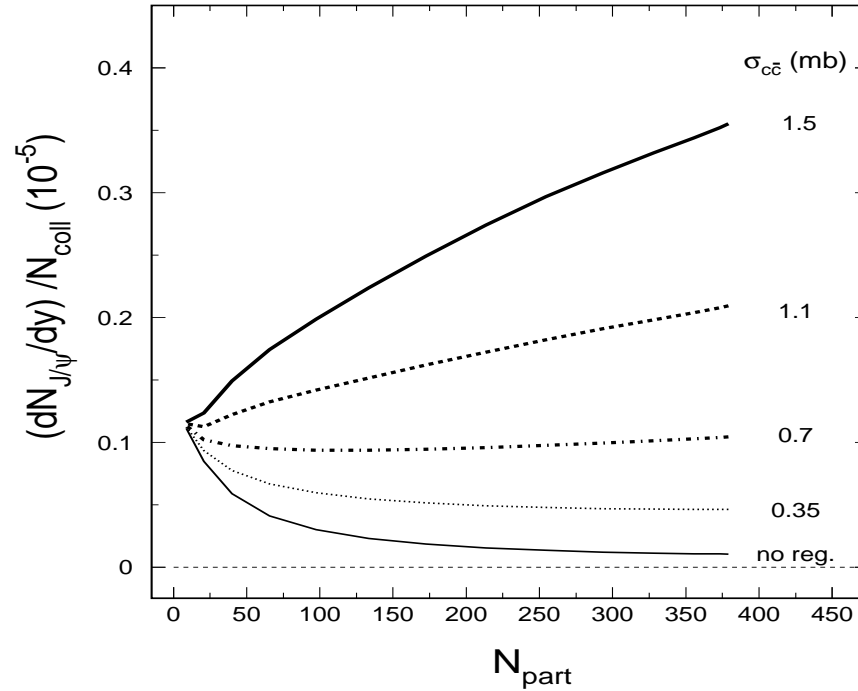
Figure 20: The effect of various values of the $c\bar{c}$ total cross section on the number of J/ψ produced per binary collision as a function of the number of participants. (With N. Xu and L. Grandchamp.)

PHENIX J/ψ pp Rapidity Distribution Close to that from pQCD

No scaling needed to obtain reasonable agreement with data
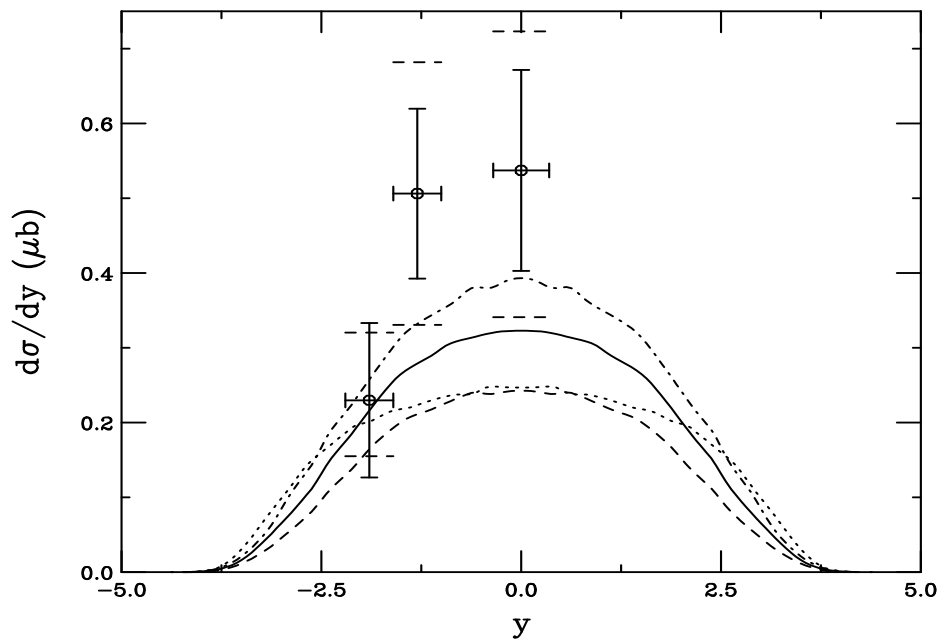
Figure 21: Direct J/ψ rapidity distributions compared to PHENIX data from Quark Matter '02. The data points are scaled to remove the $J/\psi \to l^+l^-$ branching ratio and to include direct production only. The solid curve employs the MRST HO distributions with $m = \mu/2 = 1.2$ GeV, the dashed, MRST HO with $m = \mu = 1.4$ GeV, the dot-dashed, CTEQ 5M with $m = \mu/2 = 1.2$ GeV, and the dotted, GRV 98 HO with $m = \mu = 1.3$ GeV.

Charmonium Production in the Color Evaporation Model (CEM)

All charmonium states are treated like $c\overline{c}$ below $D\overline{D}$ threshold

Distributions for all charmonium family members identical

At LO, $gg \rightarrow c\overline{c}$ and $q\overline{q} \rightarrow c\overline{c}$; NLO add $gq \rightarrow c\overline{c}q$

$$\sigma_C^{\text{CEM}} = F_C \sum_{i,j} \int_{4m^2}^{4m_D^2} d\hat{s} \int dx_1 dx_2 \; f_{i/p}(x_1, \mu^2) \; f_{j/p}(x_2, \mu^2) \; \hat{\sigma}_{ij}(\hat{s}) \; \delta(\hat{s} - x_1 x_2 s)$$

F_C fixed at NLO

Data and branching ratios can be used to separate out the F_C's for each state in quarkonium family

Values of m and μ^2 for several parton densities fixed from $c\overline{c}$ production

Forward J/ψ Production Cross Sections vs. Data

Forward J/ψ cross sections ($x_F > 0$) compared to data

Inclusive J/ψ cross section–all figures include feeddown from χ_c and ψ'

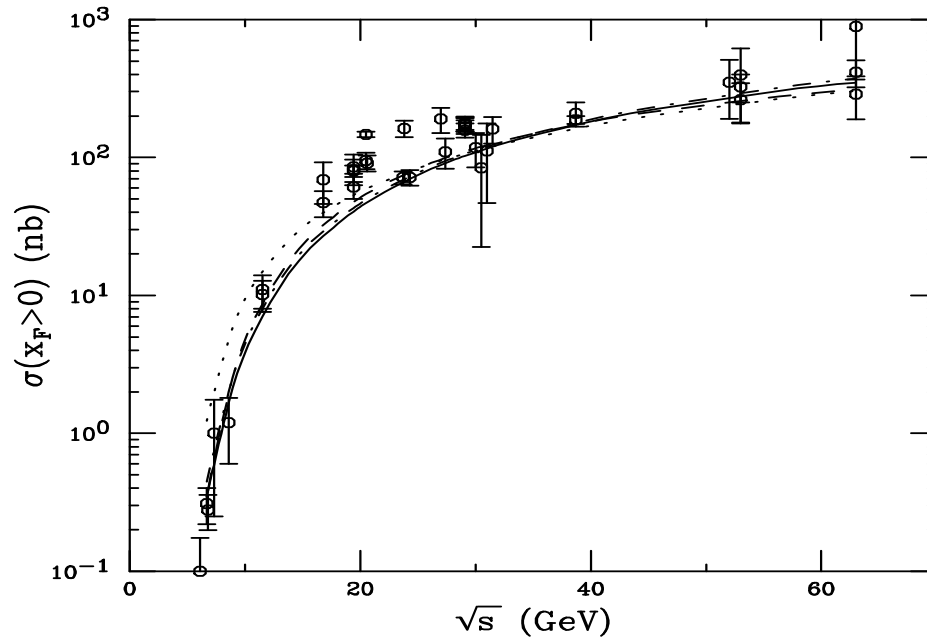Same parameters used as those that agree with $c\bar{c}$ total cross sections
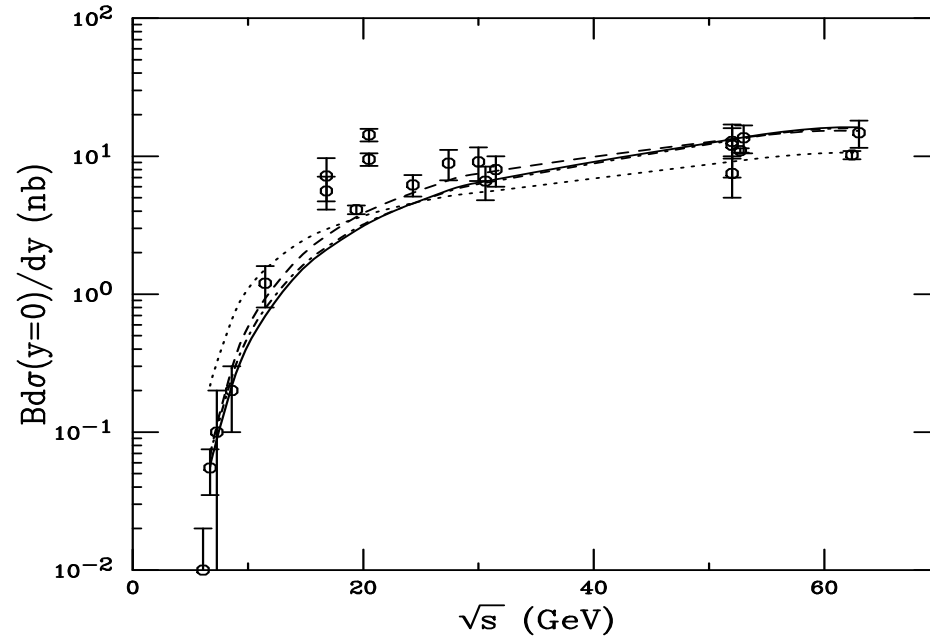

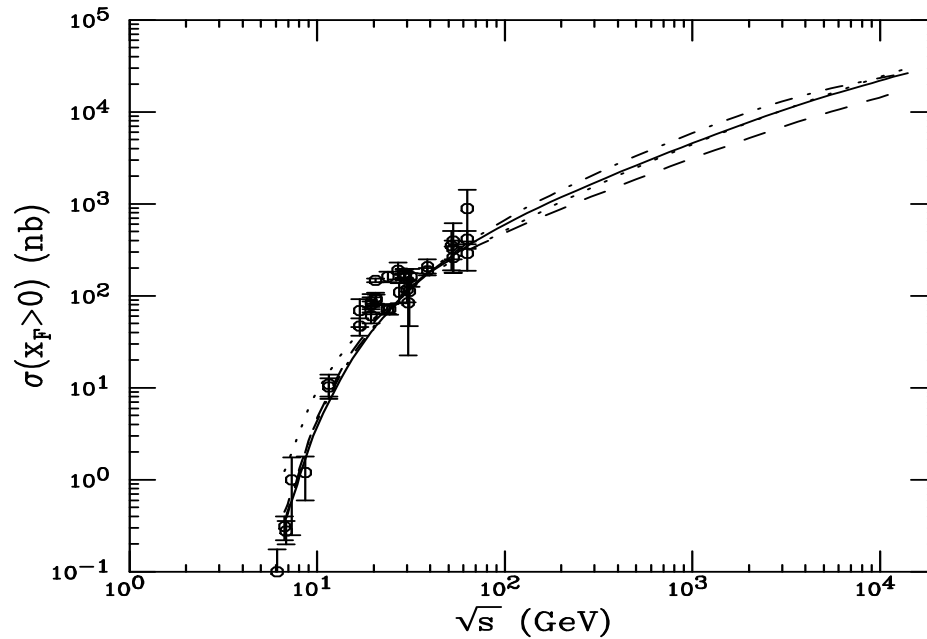Figure 22: J/ψ production data on total cross sections with $x_F > 0$ compared to NLO CEM calculations. The solid curve employs the MRST HO distributions with $m = \mu/2 = 1.2$ GeV, the dashed, MRST HO with $m = \mu = 1.4$ GeV, the dot-dashed, CTEQ 5M with $m = \mu/2 = 1.2$ GeV, and the dotted, GRV 98 HO with $m = \mu = 1.3$ GeV.

J/ψ Production Cross Sections at $y = 0$

Inclusive $J/\psi \to l^+ l^-$ cross sections compared to data

Figure 23: J/ψ production data at $y = 0$ compared to NLO CEM calculations. The solid curve employs the MRST HO distributions with $m = \mu/2 = 1.2$ GeV, the dashed, MRST HO with $m = \mu = 1.4$ GeV, the dot-dashed, CTEQ 5M with $m = \mu/2 = 1.2$ GeV, and the dotted, GRV 98 HO with $m = \mu = 1.3$ GeV.

Extrapolated J/ψ Total Cross Sections

Total forward J/ψ cross sections extrapolated to higher energy

Energy dependence obtained from NLO CEM

Factor of ~ 1.6 between results at 200 GeV

Figure 24: NLO J/ψ forward cross sections. The solid curve employs the MRST HO distributions with $m = \mu/2 = 1.2$ GeV, the dashed, MRST HO with $m = \mu = 1.4$ GeV, the dot-dashed, CTEQ 5M with $m = \mu/2 = 1.2$ GeV, and the dotted, GRV 98 HO with $m = \mu = 1.3$ GeV.

Fitted Fractions and Cross Sections for J/ψ in CEM

Case	PDF	m (GeV)	μ/m	$\sigma_{J/\psi}/\sigma_C^{\rm CEM}$
$\psi 1$	MRST HO	1.2	2	0.0144
$\psi 2$	MRST HO	1.4	1	0.0248
$\psi 3$	CTEQ 5M	1.2	2	0.0155
$\psi 4$	GRV 98 HO	1.3	1	0.0229

Table 3: The production fractions obtained from fitting the CEM cross section to the J/ψ total cross sections and $y = 0$ cross sections as a function of energy. The PDF, charm quark mass, and scales used are the same as those obtained by comparison of the $c\bar{c}$ cross section to the pp data.

Case	$\sqrt{S} = 200$ GeV					$\sqrt{S} = 5.5$ TeV				
	$\sigma_{J/\psi}^{\rm inc}$	$\sigma_{J/\psi}^{\rm dir}$	$\sigma_{\chi c1}$	$\sigma_{\chi c2}$	$\sigma_{\psi'}$	$\sigma_{J/\psi}^{\rm inc}$	$\sigma_{J/\psi}^{\rm dir}$	$\sigma_{\chi c1}$	$\sigma_{\chi c2}$	$\sigma_{\psi'}$
$\psi 1$	2.35	1.46	1.41	2.33	0.33	30.8	19.0	18.5	30.5	4.3
$\psi 2$	1.76	1.09	1.06	1.74	0.25	20.2	12.5	12.1	20.0	2.8
$\psi 3$	2.84	1.76	1.70	2.81	0.40	36.0	22.2	21.6	35.6	5.0
$\psi 4$	2.10	1.31	1.26	2.08	0.29	32.1	19.8	19.3	31.8	4.5

Table 4: The charmonium cross sections (in μb) obtained from the CEM fits for NN collisions at 200 GeV and 5.5 TeV. The inclusive and direct J/ψ cross sections are both given.

.

Extrapolated J/ψ Cross Sections at $y = 0$

Model cross sections extrapolated to RHIC energies with the preliminary PHENIX e^+e^- point at $y \sim 0$

Also shown is old Craigie parameterization, $Bd\sigma/dy|_{y=0} = 50\exp(-14.7m_{J/\psi}/\sqrt{S})$ nb
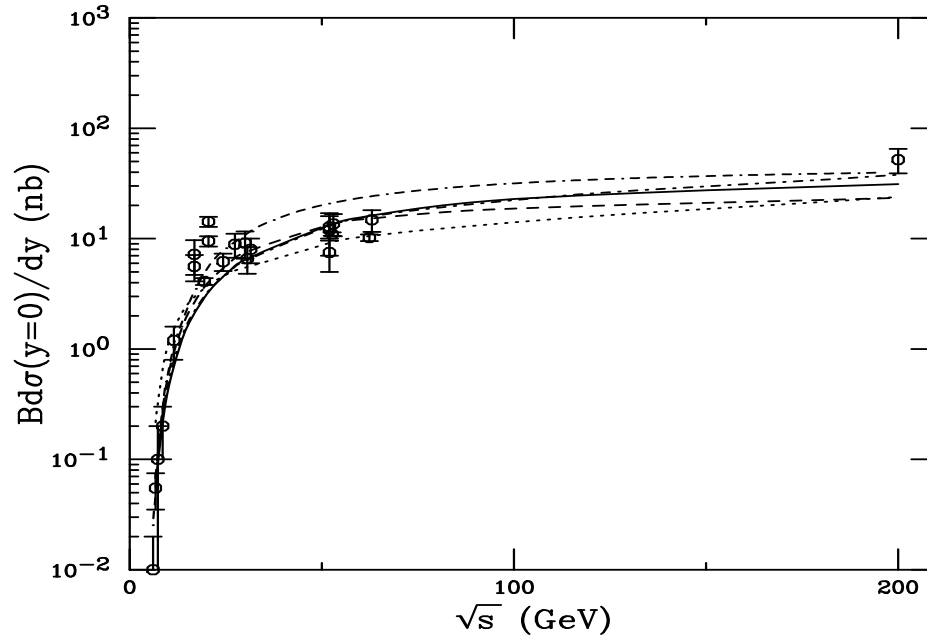

Figure 25: J/ψ production data at $y = 0$ compared to NLO CEM calculations. The solid curve employs the MRST HO distributions with $m = \mu/2 = 1.2$ GeV, the dashed, MRST HO with $m = \mu = 1.4$ GeV, the dot-dashed, CTEQ 5M with $m = \mu/2 = 1.2$ GeV, and the dotted, GRV 98 HO with $m = \mu = 1.3$ GeV. The dot-dash-dash-dashed curve is the Craigie parameterization. The PHENIX point at $y = 0$ is included.

In dA Interactions, Nuclear Effects Should Become Important

Nuclear effects seen to be important in charmonium production at fixed target energies

In extrapolated pA cross sections, the exponent α was shown to be a function of both x_F and p_T

Several mechanisms affect A dependence in cold matter, we consider two here:

- Nuclear Shadowing — initial-state effect on the parton distributions affecting the level of production, important as a function of rapidity/x_F

- Absorption — final-state effect, after $c\bar{c}$ that forms the J/ψ has been produced, pair breaks up in matter due to interactions with nucleons

Nuclear Shadowing

.

Modification of parton distributions in large nuclei measured in nuclear DIS.

Source of modification?

- Recombination of long wavelength partons

- Multiple interactions along parton path, coherence length $l_c \sim 1/2mx$

Neither can explain effect over all x.

Spatial dependence of shadowing? Partons near nuclear surface should feel weaker shadowing effect:

- Lower probability for recombination

- Reduced path length in matter near surface

Form of spatial dependence?

- If recombination or $l_c < R_A$, shadowing proportional to local nuclear density.

- If $l_c > R_A$, shadowing proportional to parton path through nucleus.

.

Nuclear Parton Distributions

Nuclear parton densities

$$F_i^A(x, Q^2, \vec{r}, z) = \rho_A(s) S^i(A, x, Q^2, \vec{r}, z) f_i^N(x, Q^2) s = \sqrt{b^2 + z^2}$$

$$\rho_A(s) = \rho_0 \frac{1 + \omega(s/R_A)^2}{1 + \exp[(s - R_A)/d]}$$

We use EKS98 and Frankfurt, Guzey and Strickman (FGS) parameterizations

EKS98 has no spatial dependence, FGS inhomogeneous parameterization recently made available — results here with FGS will eventually be replaced by their own parameterization

With no nuclear modifications, $S^i(A, x, Q^2, \vec{r}, z) \equiv 1$.

Spatial dependence of shadowing

Proportional to local nuclear density:

$$S_{\text{WS}}^i = S^i(A, x, Q^2, \vec{r}, z) = 1 + N_{\text{WS}}[S^i(A, x, Q^2) - 1]\frac{\rho(s)}{\rho_0}$$

Proportional to nuclear path length:

$$S_\rho^i(A, x, Q^2, \vec{r}, z) = 1 + N_\rho(S^i(A, x, Q^2) - 1) \int dz \rho_A(\vec{r}, z) \ .$$

Normalization: $(1/A) \int d^2 r dz \rho_A(s) S_{\text{WS, R}}^i \equiv S^i$. Larger than average modifications for $b = 0$. Nucleons like free protons when $s \gg R_A$.

Comparing Shadowing Parameterizations

Recent parameterization by Frankfurt *et al* also shown, uses EKS98 for valence shadowing, stronger gluon shadowing at low x, cuts off modification above $x = 0.25$ for sea, 0.03 for gluon
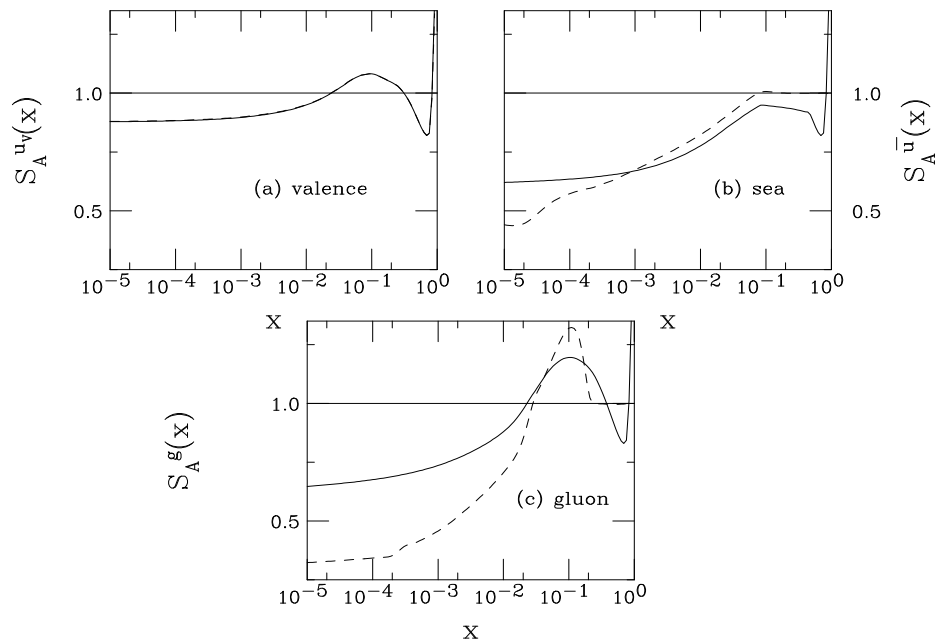
Figure 26: The EKS98 and FGS shadowing parameterizations are compared at the scale $\mu = 2m = 2.4$ GeV. The solid curves are the EKS98 parameterization, the dashed, FGS.

Effect on J/ψ pAu/pp Ratios

Ratios at LO with MRST LO PDFs and the NLO ratios with MRST HO PDFs give similar results

Frankfurt *et al* parameterization has a bigger effect at large rapidity
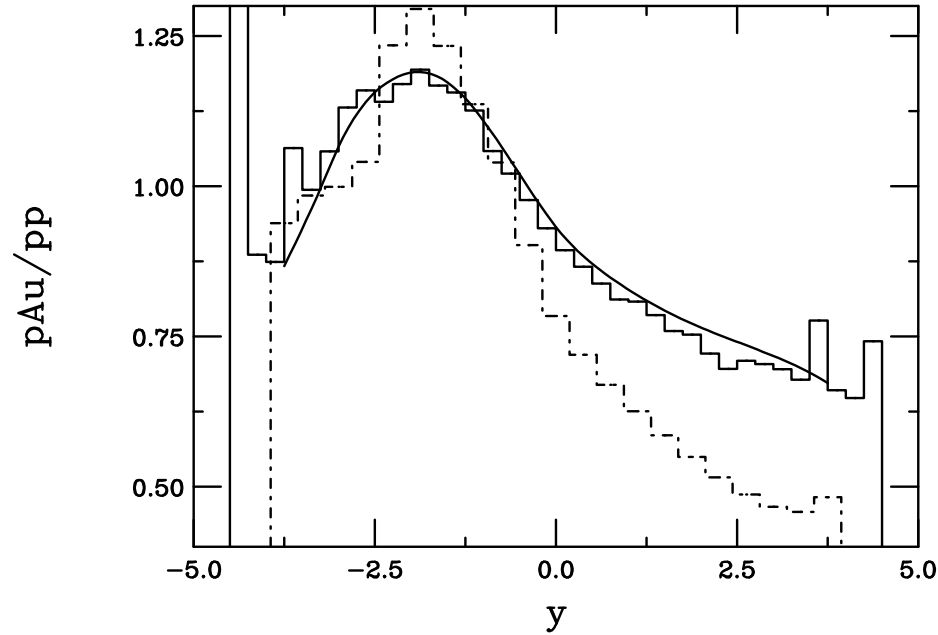
Figure 27: The J/ψ pAu/pp ratio at 200 GeV at NLO (solid histogram, using the MRST HO distributions with $m = \mu/2 = 1.2$ GeV), at LO (solid curve using the MRST LO distributions with the same mass and scale) calculated with the EKS98 parameterization are compared. The ratio with the same parameters and the FGS shadowing parameterization is given in the dashed histogram.

Rapidity Dependence in dA, 4 b Bins

Stronger shadowing for central impact parameters, reduced effect in peripheral bins

Results integrated over all b equivalent to homogeneous shadowing, as expected
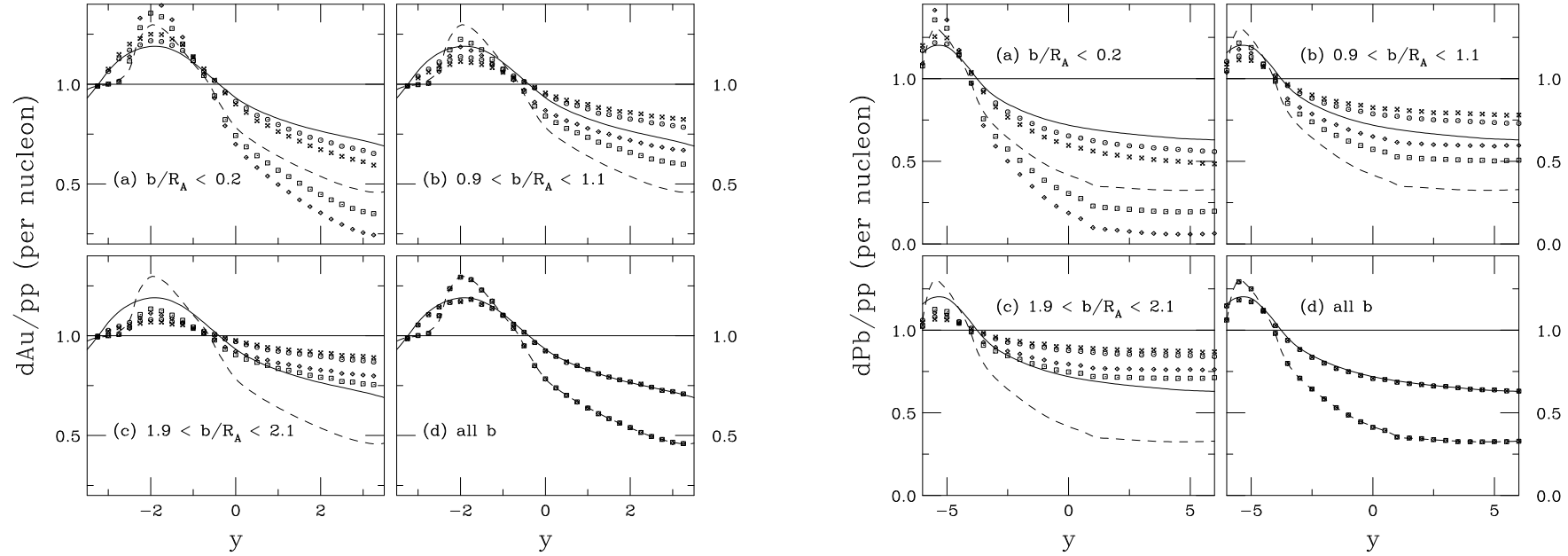
Figure 28: The J/ψ dA/pp ratio at 200 GeV (left) and 6.2 TeV (right) as a function of rapidity. The results are shown for the EKS98 (solid line for homogeneous shadowing, circles and x's for inhomogeneous shadowing assuming local density and nuclear path length respectively) and FGS (dashed line for homogeneous shadowing, squares and diamonds for inhomogeneous shadowing assuming local density and nuclear path length respectively). The calculation is at LO with the MRST LO parton densities, $m = \mu/2 = 1.2$ GeV. The bins are (a) $b/R_A < 0.2$, (b) $0.9 < b/R_A < 1.1$, (c) $1.9 < b/R_A < 2.1$ and (d) all b.

Effect Sizable in Central/Peripheral Ratio

Larger effect for FGS than EKS98

Path length assumption gives larger central/peripheral effect
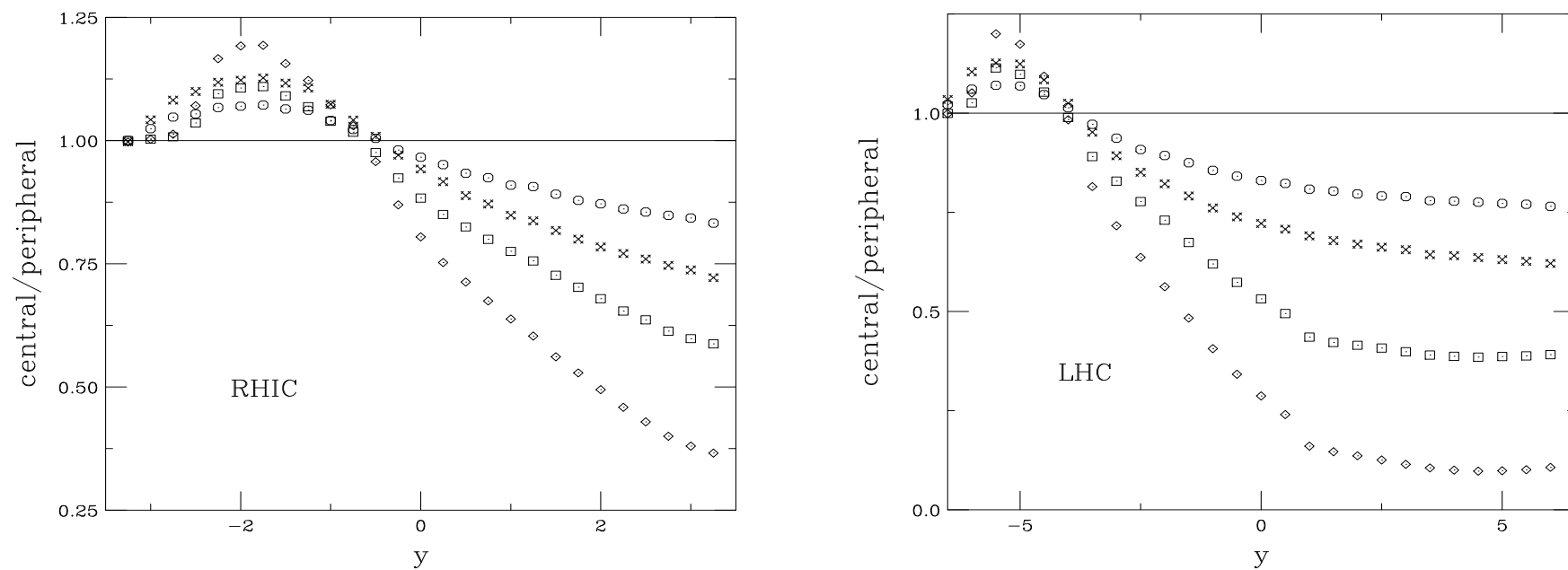
Figure 29: The J/ψ inhomogeneous shadowing ratio in central ($b/R_A < 0.2$) vs. peripheral ($0.9 < b/R_A < 1.1$) at 200 GeV (left) and 6.2 TeV (right) as a function of rapidity. The results are shown for the EKS98 (circles and x's for local density and nuclear path length respectively) and FGS (squares and diamonds for local density and nuclear path length respectively).

PHENIX J/ψ Data Show Modification of Nuclear PDFs

Little effect at midrapidity but suppression seen at forward η

Nuclear shadowing alone gives fair agreement with data but absorption still needs to be included on a reasonable level   .
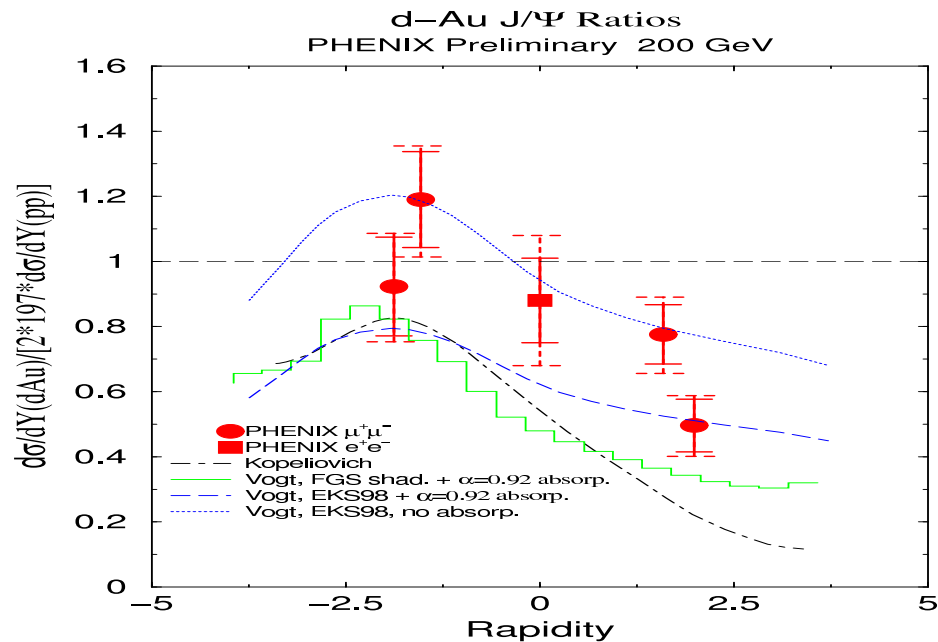
Figure 30: PHENIX d+Au/pp ratio for J/ψ production as a function of rapidity. The curves are theory calculations. The upper curve is EKS98 shadowing with no absorption. The lower shadowing curves have nuclear absorption added in by scaling the shadowing curves by A^α with $\alpha = 0.92$. [From PHENIX Collaboration, QM'04 proceedings.]

48

J/ψ **Absorption by Nucleons**

Woods-Saxon nuclear density profiles typically used

$$
\begin{aligned}
\sigma_{pA} &= \sigma_{pN} \int d^2b \int_{-\infty}^{\infty} dz\, \rho_A(b,z) S_A^{\rm abs}(b) \\
&= \sigma_{pN} \int d^2b \int_{-\infty}^{\infty} dz\, \rho_A(b,z) \exp\left\{-\int_z^{\infty} dz'\, \rho_A(b,z')\sigma_{\rm abs}(z'-z)\right\}
\end{aligned}
$$

Note that if $\rho_A = \rho_0$, $\alpha = 1 - 9\sigma_{\rm abs}/(16\pi r_0^2)$

We discuss absorption of color singlet and color octet states in the CEM and a combination of the two in NRQCD

Singlet Absorption Model

All $c\bar{c}$ pairs assumed to be produced in small color singlet states

Assume quadratic growth of cross section with proper time until formation time τ_F (Blaizot and Ollitrault)

Strongest at low to negative x_F where J/ψ can form in the target

Asymptotic ψ' and χ_c cross sections proportional to the final state meson size, *e.g.* $\sigma^{\mathrm{s}}_{\psi'N} = \sigma^{\mathrm{s}}_{J/\psi N}(r_{\psi'}/r_{J/\psi})^2$ (Povh and Hüfner)

$$\sigma_{\mathrm{abs}}(z' - z) = \begin{cases} \sigma^{\mathrm{s}}_{CN}(\dfrac{\tau}{\tau_F^C})^2 & \text{if } \tau < \tau_F^C \\[2ex] \sigma^{\mathrm{s}}_{CN} & \text{otherwise} \end{cases} .$$

$$\tau_F^{J/\psi} = 0.92 \text{ fm} \qquad \sigma^{\mathrm{s}}_{J/\psi N} \sim 2.5 \text{ mb}$$
$$\tau_F^{\psi'} = 1.5 \text{ fm} \qquad \sigma^{\mathrm{s}}_{\psi'N} = 3.7\,\sigma^{\mathrm{s}}_{J/\psi N}$$
$$\tau_F^{\chi_c} = 2 \text{ fm} \qquad \sigma^{\mathrm{s}}_{\chi_c N} = 2.4\,\sigma^{\mathrm{s}}_{J/\psi N}$$

A Dependence of 'Color Transparency'

All states produced outside target for $x_F \geq 0$ at 920 GeV (no absorption)

Strong decrease at negative x_F expected in this model for all states but need high statistics to distinguish between them
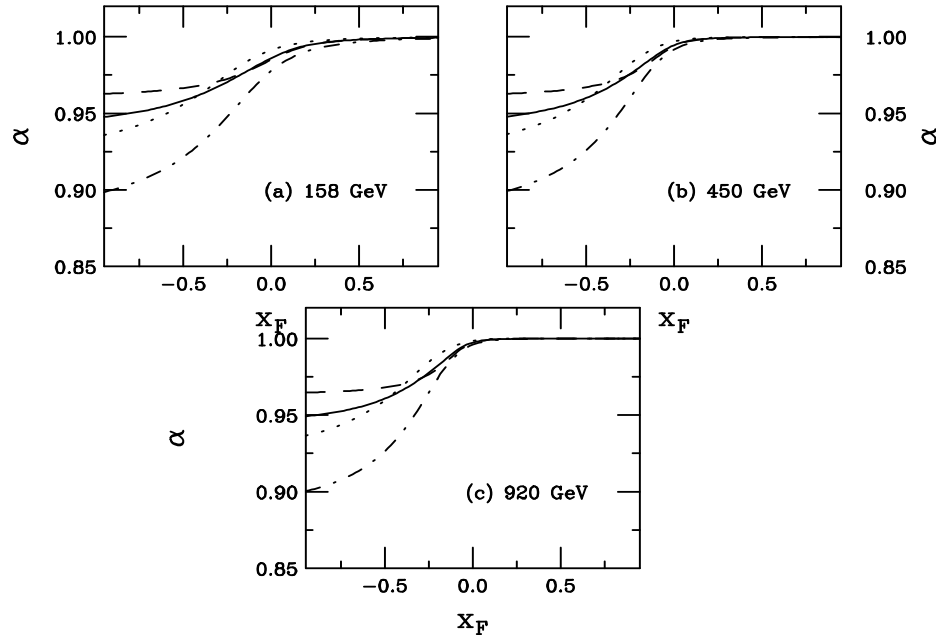
Figure 31: The *A* dependence of singlet absorption is shown for 158 (a), 450 (b), and 920 (c) GeV interactions. The total J/ψ (solid), direct J/ψ (dashed), ψ' (dot-dashed) and χ_c (dotted) dependencies are shown. [From R.V., Nucl. Phys. **A700** (2002) 539.]

Octet Absorption Model

Pre-resonant $c\bar{c}$ pairs travel through the nucleus as $|(c\bar{c})_8 g\rangle$ color octet states

Characteristic octet lifetime $\tau_8 \sim 0.25$ fm

For $x_F \geq -0.1$, path length of $|(c\bar{c})_8 g\rangle$ through the target from its production point is greater than maximum path length

These fast states pass through nucleus in color octets so that the pre-resonant A dependence is the same for J/ψ, ψ' and χ_c (Kharzeev and Satz) — $\sigma_{\rm abs}^{\rm o} = 3$ mb agrees with E866 forward A dependence

Universal constant absorption cross section usually assumed for nuclear collision studies (NA38, NA50) where $0 < x_F < 0.18$

At negative x_F, path length is shorter and octet state can neutralize its color inside target and be absorbed as color singlet

Only J/ψ likely to be fully formed inside target even though color neutralization may occur for all states

A Dependence of Octet Absorption

Dependencies different at large negative x_F where neutralization occurs

All values of α identical when state passes through target as octet

As energy increases, color neutralization occurs at more negative x_F
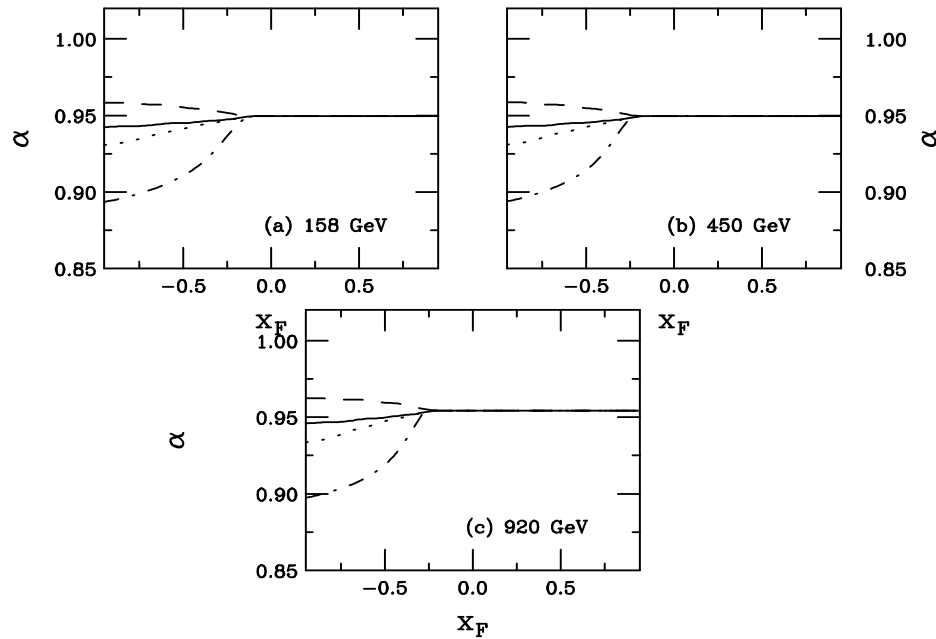
Figure 32: The A dependence of octet absorption at 158 (a), 450 (b), and 920 (c) GeV interactions. The total J/ψ (solid), direct J/ψ (dashed), ψ' (dot-dashed) and χ_c (dotted) dependencies are shown. [From R.V., Nucl. Phys. **A700** (2002) 539.]

Singlet + Octet Absorption

Relative contributions of singlet and octet production set by NRQCD (Zhang *et al.*)

Equal absorption cross sections for all octet states

Singlet cross sections set by final state size

$$\frac{d\sigma_{pA}^{\psi}}{dx_F} = \int d^2b \left[\frac{d\sigma_{pp}^{\psi,\,\mathrm{oct}}}{dx_F} T_A^{\psi,\mathrm{eff\,(oct)}}(b) + \frac{d\sigma_{pp}^{\psi,\,\mathrm{sing}}}{dx_F} T_A^{\psi,\mathrm{eff\,(sing)}}(b) \right] \,,$$

$$\frac{d\sigma_{pA}^{\chi_{cJ} \to J/\psi X}}{dx_F} = \int d^2b \sum_{J=0}^{2} B(\chi_{cJ} \to J/\psi X) \left[\frac{d\sigma_{pp}^{\chi_{cJ},\,\mathrm{oct}}}{dx_F} T_A^{\chi_{cJ},\mathrm{eff\,(oct)}}(b) + \frac{d\sigma_{pp}^{\chi_{cJ},\,\mathrm{sing}}}{dx_F} T_A^{\chi_{cJ},\mathrm{eff\,(sing)}}(b) \right] \,,$$

$$\frac{d\sigma_{pA}^{J/\psi,\,\mathrm{tot}}}{dx_F} = \int d^2b \left\{ \left[\frac{d\sigma_{pp}^{J/\psi,\,\mathrm{dir,\,oct}}}{dx_F} T_A^{J/\psi,\mathrm{eff\,(oct)}}(b) \right. \right.$$

$$+ \sum_{J=0}^{2} B(\chi_{cJ} \to J/\psi X) \frac{d\sigma_{pp}^{\chi_{cJ},\,\mathrm{oct}}}{dx_F} T_A^{\chi_{cJ},\mathrm{eff\,(oct)}}(b) + B(\psi' \to \psi X) \frac{d\sigma_{pp}^{\psi',\,\mathrm{oct}}}{dx_F} T_A^{\chi_{cJ},\mathrm{eff\,(oct)}}(b) \Bigg]$$

$$+ \left[\frac{d\sigma_{pp}^{J/\psi,\,\mathrm{dir,\,sing}}}{dx_F} T_A^{J/\psi,\mathrm{dir,eff\,(sing)}}(b) + \sum_{J=0}^{2} B(\chi_{cJ} \to \psi X) \frac{d\sigma_{pp}^{\chi_{cJ},\,\mathrm{sing}}}{dx_F} T_A^{\chi_{cJ},\,\mathrm{eff\,(sing)}}(b) \right.$$

$$+ B(\psi' \to \psi X) \frac{d\sigma_{pp}^{\psi',\,\mathrm{sing}}}{dx_F} T_A^{\psi',\,\mathrm{eff\,(sing)}}(b) \Bigg] \Bigg] \Bigg\}$$

$$T_A^{\mathrm{eff}}(b) = \int_{-\infty}^{\infty} dz\, \rho_A(b,z) \exp \left\{ - \int_{z}^{\infty} dz' \rho_A(b,z') \sigma_{\mathrm{abs}}(z'-z) \right\}$$

A Dependence of Combination Model

Total J/ψ and ψ' *A* dependence very similar for $0 < x_F < 0.5$ (previously measured region)

Strong octet component of direct J/ψ makes α nearly constant

Singlet contribution to χ_c means $\alpha \sim 1$ for $0 < x_F < 0.5$
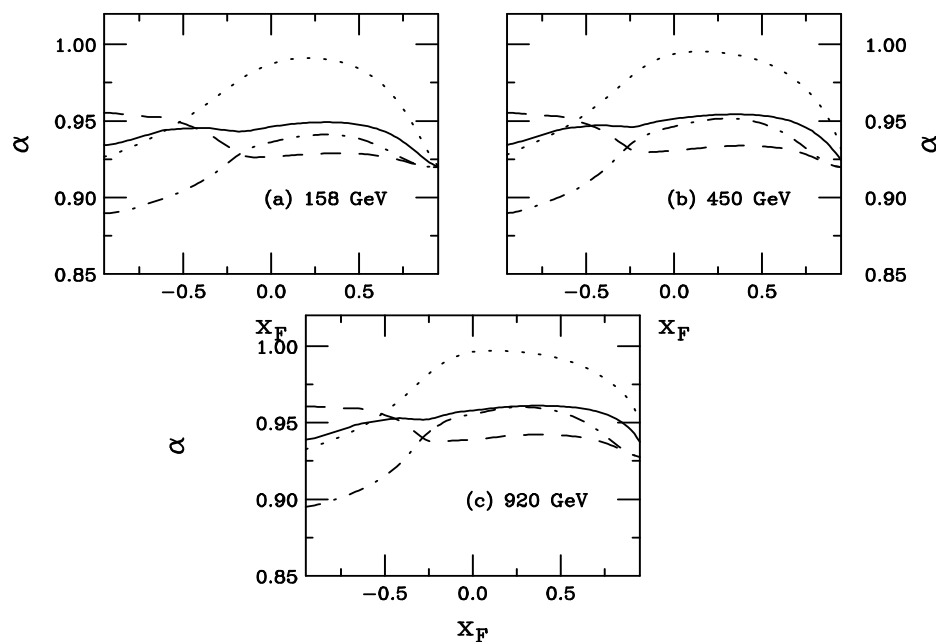
$\alpha(x_F)$ depends on relative octet/singlet contributions

Figure 33: The *A* dependence of singlet and octet absorption is shown at 158 (a), 450 (b), and 920 (c) GeV. The total J/ψ (solid), direct J/ψ (dashed), ψ' (dot-dashed) and χ_c (dotted) dependencies are shown. [From R.V., Nucl. Phys. **A700** (2002) 539.]

Including Absorption with Shadowing at RHIC

Effect of changing σ_{abs} is shown for the various absorption models

Little difference between constant and growing octet, only at large negative rapidity, singlet absorption only effective for $y < -2$
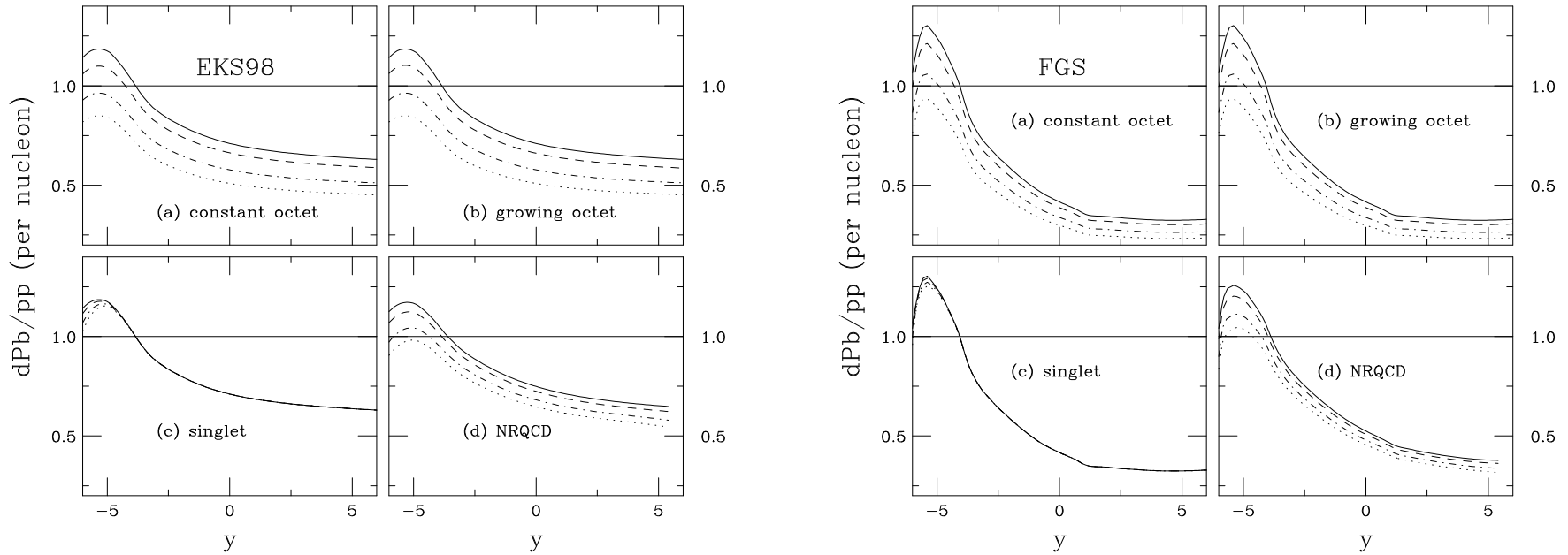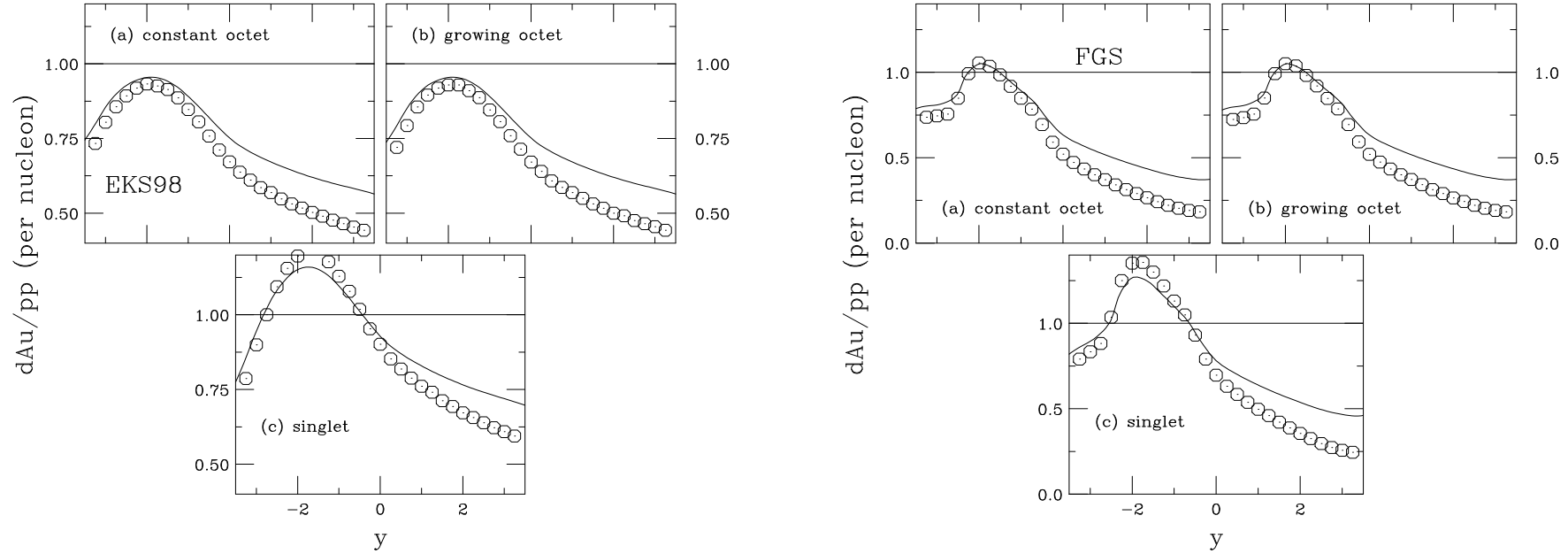.

Figure 34: The J/ψ dAu/pp ratio at 200 GeV with EKS98 (left) and FGS (right) shadowing as a function of rapidity for (a) constant octet (assuming all states have a constant cross section and do not hadronize in the nucleus), (b) growing octet (states behave as singlets if they materialize in the medium), (c) singlet, all calculated in the CEM and (d) NRQCD with a combination of octet and singlet matrix elements. For (a)-(c), the curves are no absorption (solid), $\sigma_{\mathrm{abs}} = 1$ (dashed), 3 (dot-dashed) and 5 mb (dotted). For (d), the results are shown for no absorption (solid, note slight difference relative to the CEM), 1 mb octet/1 mb singlet (dashed), 3 mb octet/3 mb singlet (dot-dashed), and 5 mb octet/3 mb singlet (dotted).

Including Absorption and Shadowing at the LHC

J/ψ not produced inside nucleus except for $y < -5$, no difference between constant and growing octet

Potentially very large J/ψ suppression at $y > -2$, particularly for FGS, even without absorption
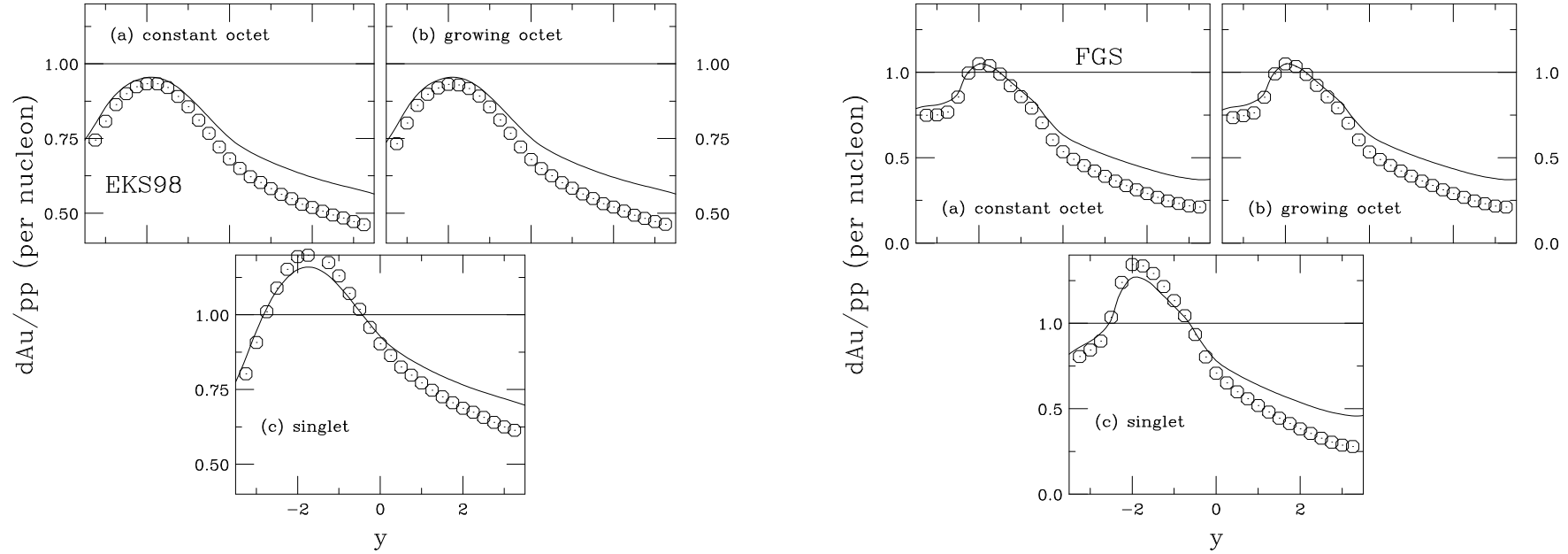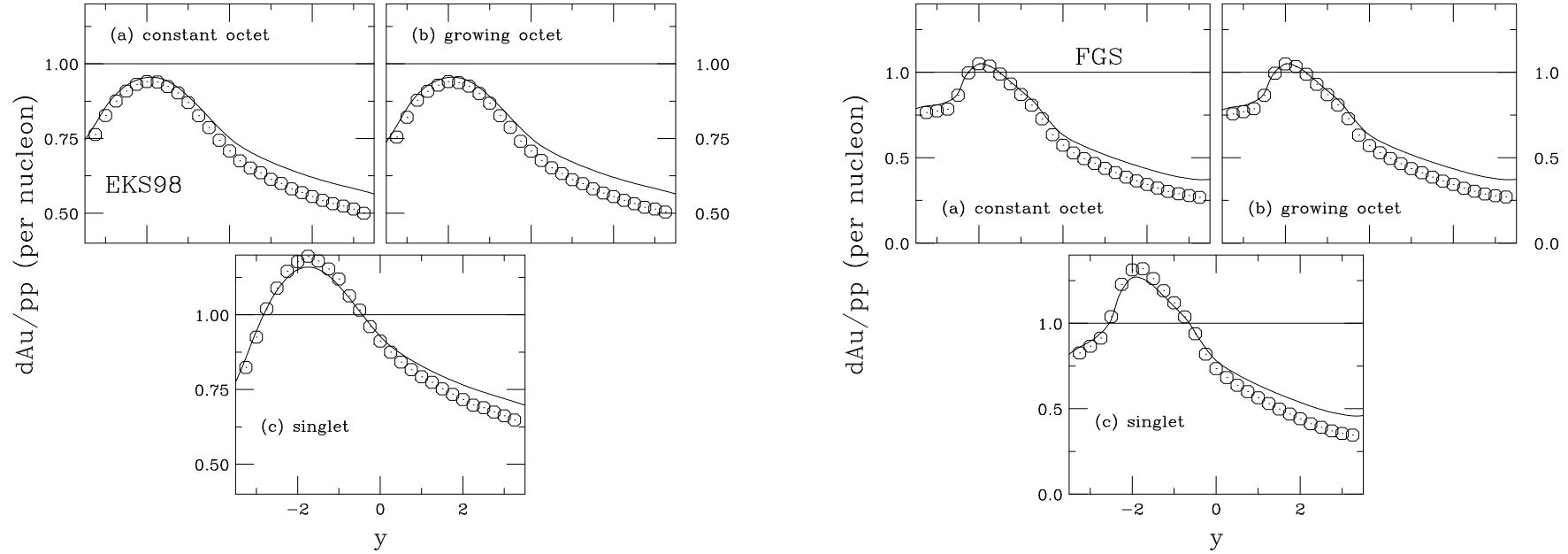
.

Figure 35: The J/ψ dAu/pp ratio at 5.5 TeV with EKS98 (left) and FGS (right) shadowing as a function of rapidity for (a) constant octet (assuming all states have a constant cross section and do not hadronize in the nucleus), (b) growing octet (states behave as singlets if they materialize in the medium), (c) singlet, all calculated in the CEM and (d) NRQCD with a combination of octet and singlet matrix elements. For (a)-(c), the curves are no absorption (solid), $\sigma_{abs} = 1$ (dashed), 3 (dot-dashed) and 5 mb (dotted). For (d), the results are shown for no absorption (solid, note slight difference relative to the CEM), 1 mb octet/1 mb singlet (dashed), 3 mb octet/3 mb singlet (dot-dashed), and 5 mb octet/3 mb singlet (dotted).

Inhomogeneous Shadowing and Absorption at RHIC

$$0 < b/R_A < 0.2$$

Figure 36: The J/ψ dAu/pp ratio at 200 GeV with EKS98 (left) and FGS (right) shadowing as a function of rapidity for (a) constant octet (assuming all states have a constant cross section and do not hadronize in the nucleus), (b) growing octet (states behave as singlets if they materialize in the medium), (c) singlet, all calculated in the CEM. The solid curves are the homogenous results while the points are impact parameter dependent shadowing, proportional to the path length, and absorption.

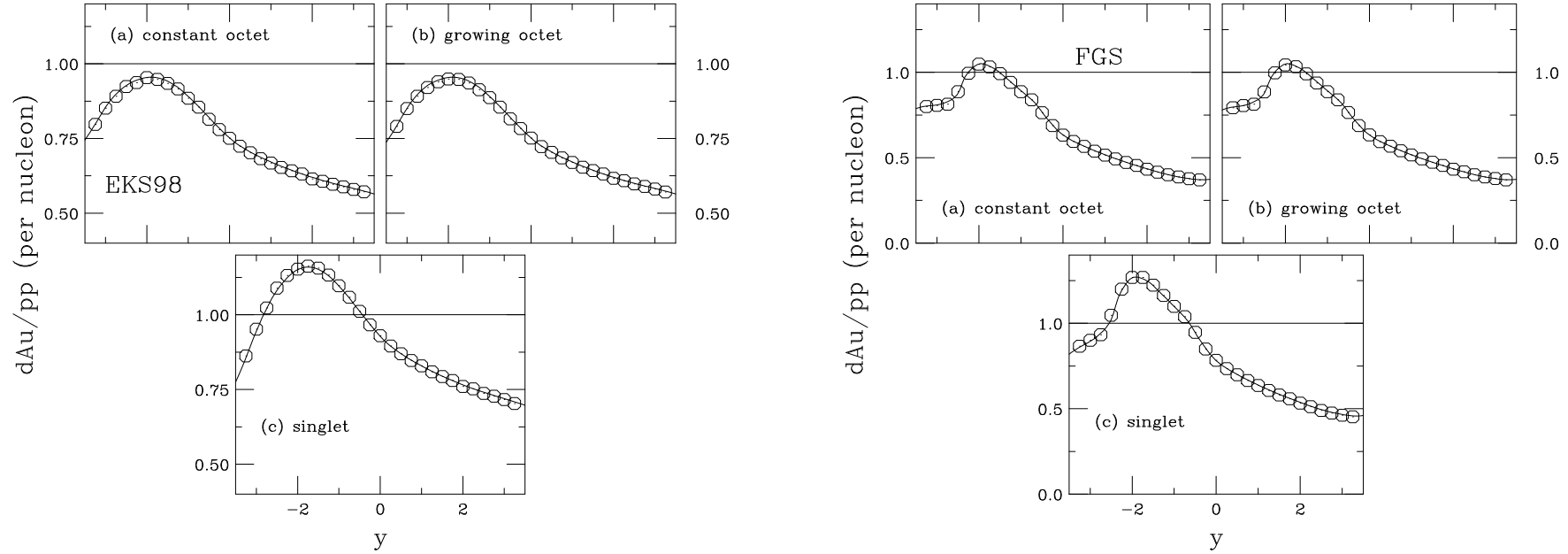# Inhomogeneous Shadowing and Absorption at RHIC

$$0.2 < b/R_A < 0.4$$

Figure 37: The J/ψ dAu/pp ratio at 200 GeV with EKS98 (left) and FGS (right) shadowing as a function of rapidity for (a) constant octet (assuming all states have a constant cross section and do not hadronize in the nucleus), (b) growing octet (states behave as singlets if they materialize in the medium), (c) singlet, all calculated in the CEM. The solid curves are the homogenous results while the points are impact parameter dependent shadowing, proportional to the path length, and absorption.

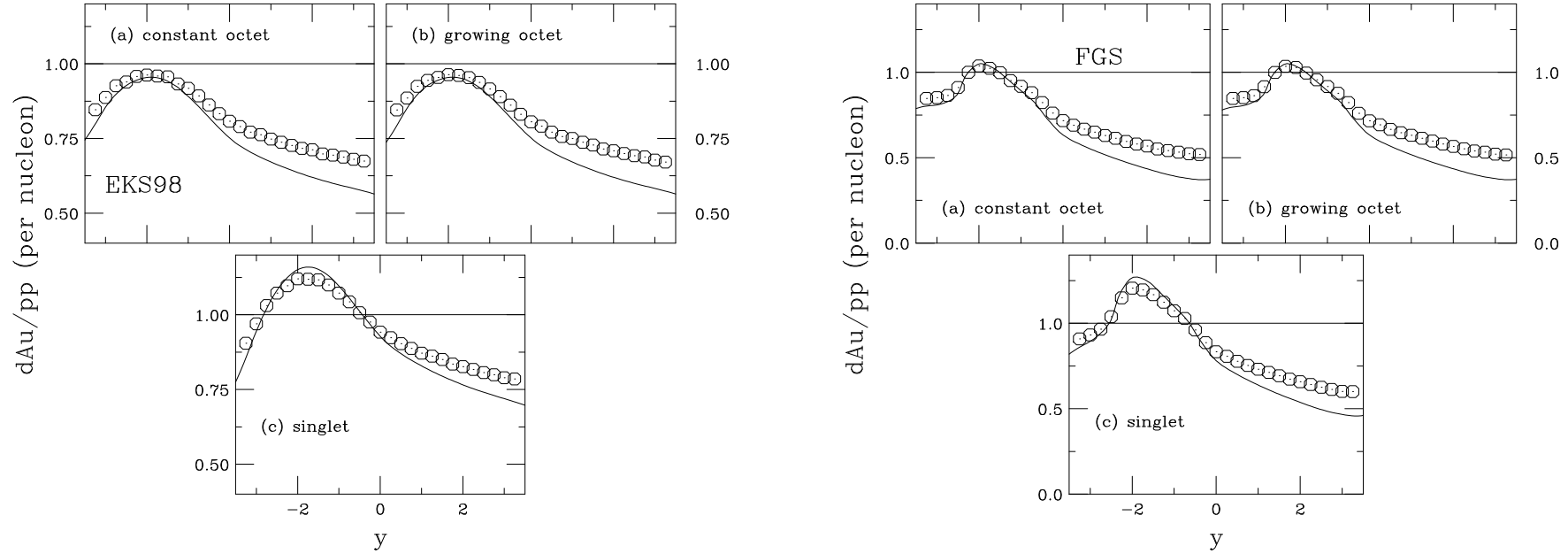# Inhomogeneous Shadowing and Absorption at RHIC

$$0.4 < b/R_A < 0.6$$

Figure 38: The J/ψ dAu/pp ratio at 200 GeV with EKS98 (left) and FGS (right) shadowing as a function of rapidity for (a) constant octet (assuming all states have a constant cross section and do not hadronize in the nucleus), (b) growing octet (states behave as singlets if they materialize in the medium), (c) singlet, all calculated in the CEM. The solid curves are the homogenous results while the points are impact parameter dependent shadowing, proportional to the path length, and absorption.

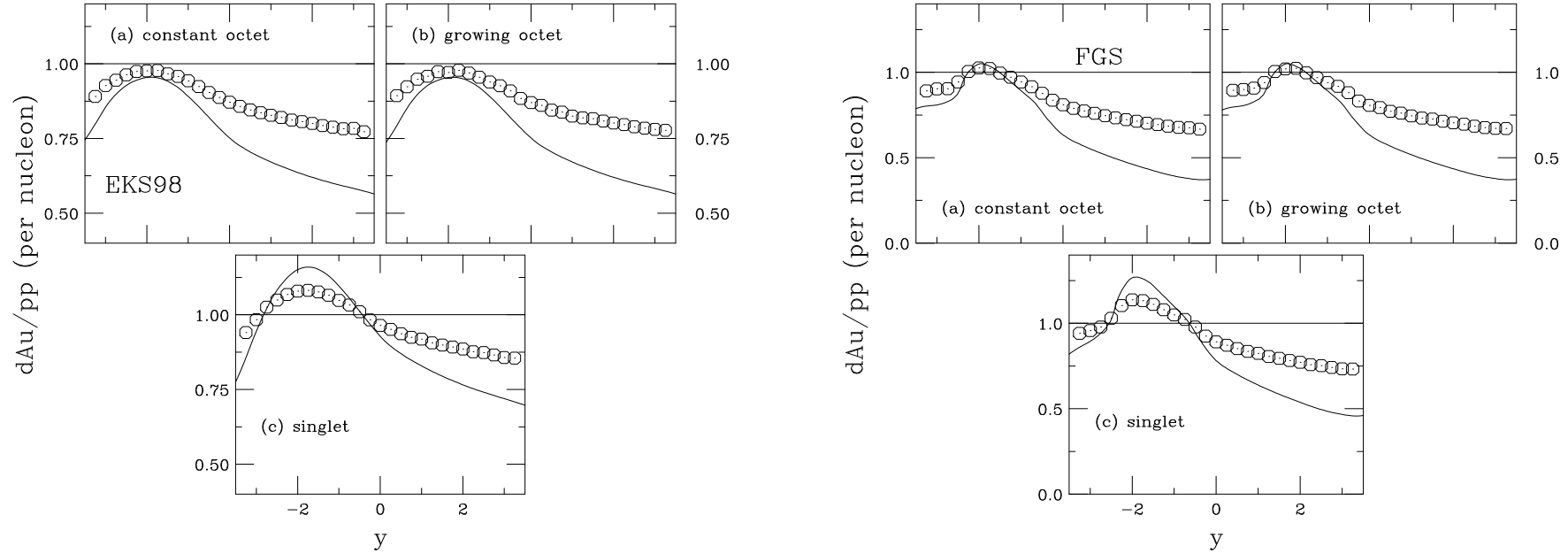# Inhomogeneous Shadowing and Absorption at RHIC

$$0.6 < b/R_A < 0.8$$

Figure 39: The J/ψ dAu/pp ratio at 200 GeV with EKS98 (left) and FGS (right) shadowing as a function of rapidity for (a) constant octet (assuming all states have a constant cross section and do not hadronize in the nucleus), (b) growing octet (states behave as singlets if they materialize in the medium), (c) singlet, all calculated in the CEM. The solid curves are the homogenous results while the points are impact parameter dependent shadowing, proportional to the path length, and absorption.

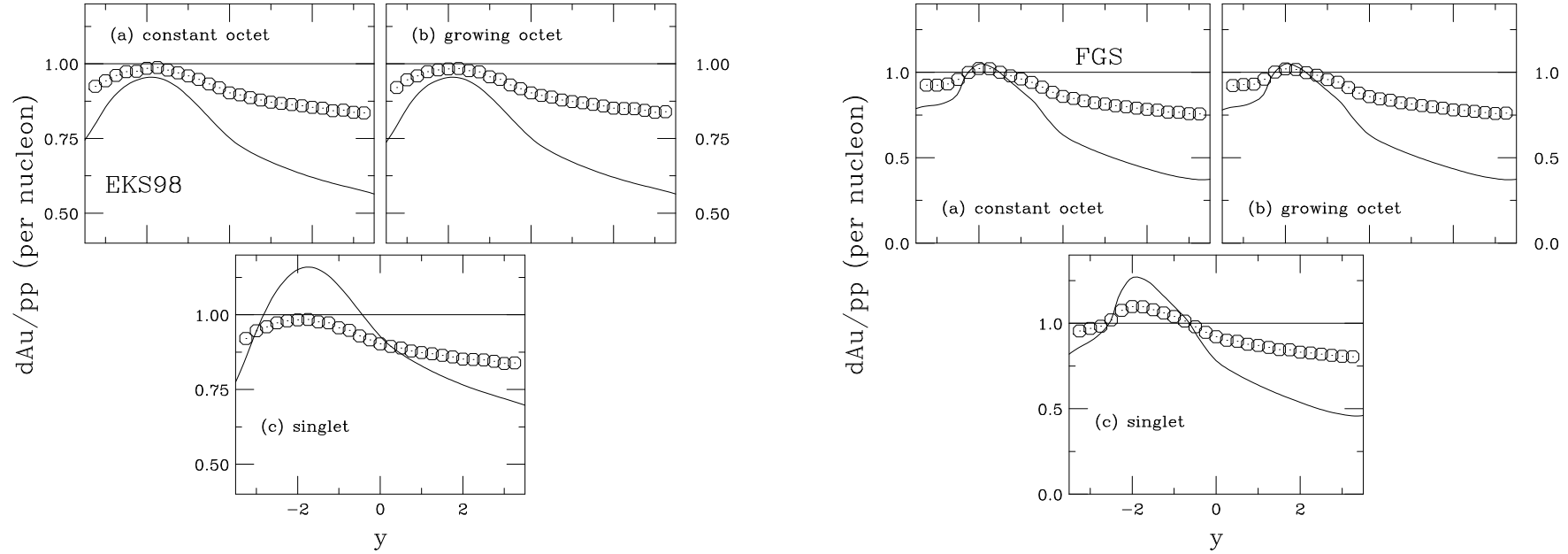# Inhomogeneous Shadowing and Absorption at RHIC

$$0.8 < b/R_A < 1.0$$

Figure 40: The J/ψ dAu/pp ratio at 200 GeV with EKS98 (left) and FGS (right) shadowing as a function of rapidity for (a) constant octet (assuming all states have a constant cross section and do not hadronize in the nucleus), (b) growing octet (states behave as singlets if they materialize in the medium), (c) singlet, all calculated in the CEM. The solid curves are the homogenous results while the points are impact parameter dependent shadowing, proportional to the path length, and absorption.

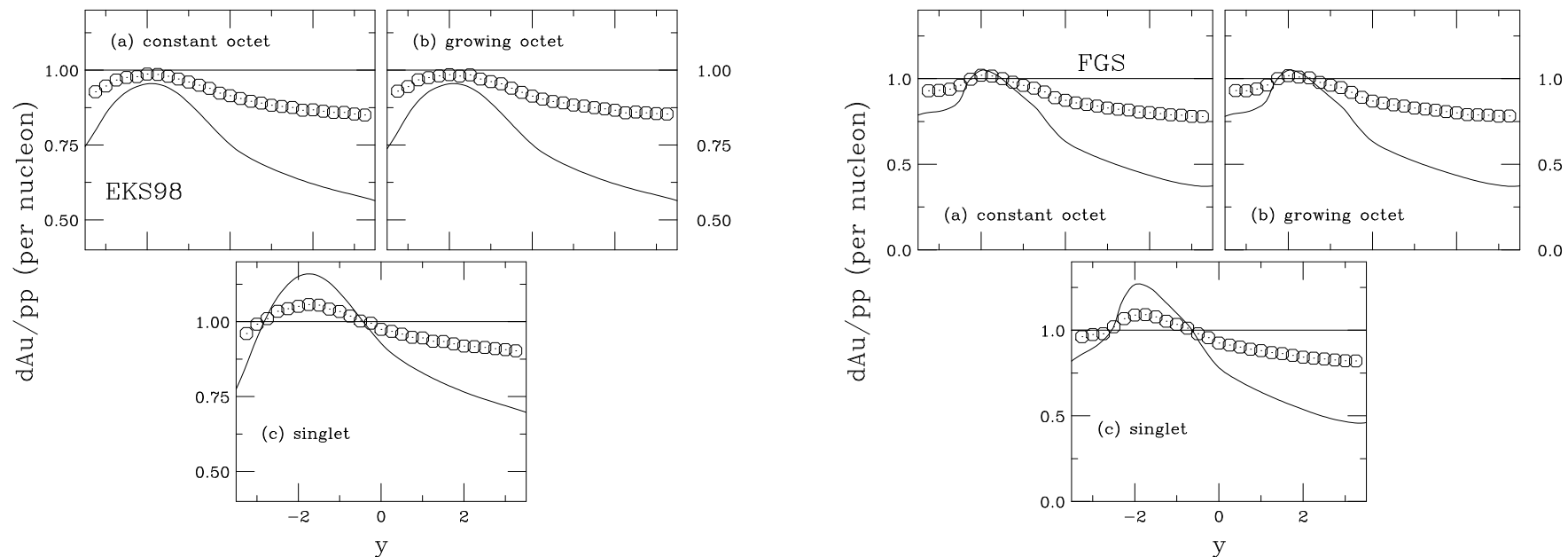# Inhomogeneous Shadowing and Absorption at RHIC

$$1.0 < b/R_A < 1.2$$

Figure 41: The J/ψ dAu/pp ratio at 200 GeV with EKS98 (left) and FGS (right) shadowing as a function of rapidity for (a) constant octet (assuming all states have a constant cross section and do not hadronize in the nucleus), (b) growing octet (states behave as singlets if they materialize in the medium), (c) singlet, all calculated in the CEM. The solid curves are the homogenous results while the points are impact parameter dependent shadowing, proportional to the path length, and absorption.

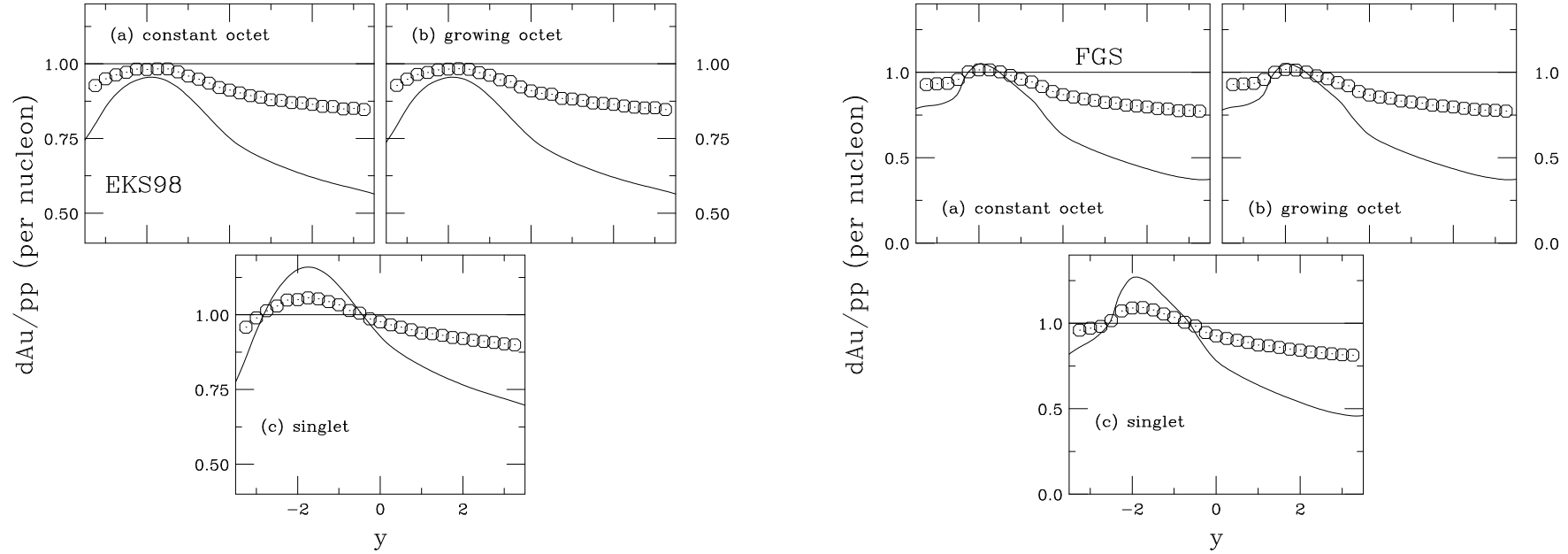# Inhomogeneous Shadowing and Absorption at RHIC

$$1.2 < b/R_A < 1.4$$

Figure 42: The J/ψ dAu/pp ratio at 200 GeV with EKS98 (left) and FGS (right) shadowing as a function of rapidity for (a) constant octet (assuming all states have a constant cross section and do not hadronize in the nucleus), (b) growing octet (states behave as singlets if they materialize in the medium), (c) singlet, all calculated in the CEM. The solid curves are the homogenous results while the points are impact parameter dependent shadowing, proportional to the path length, and absorption.

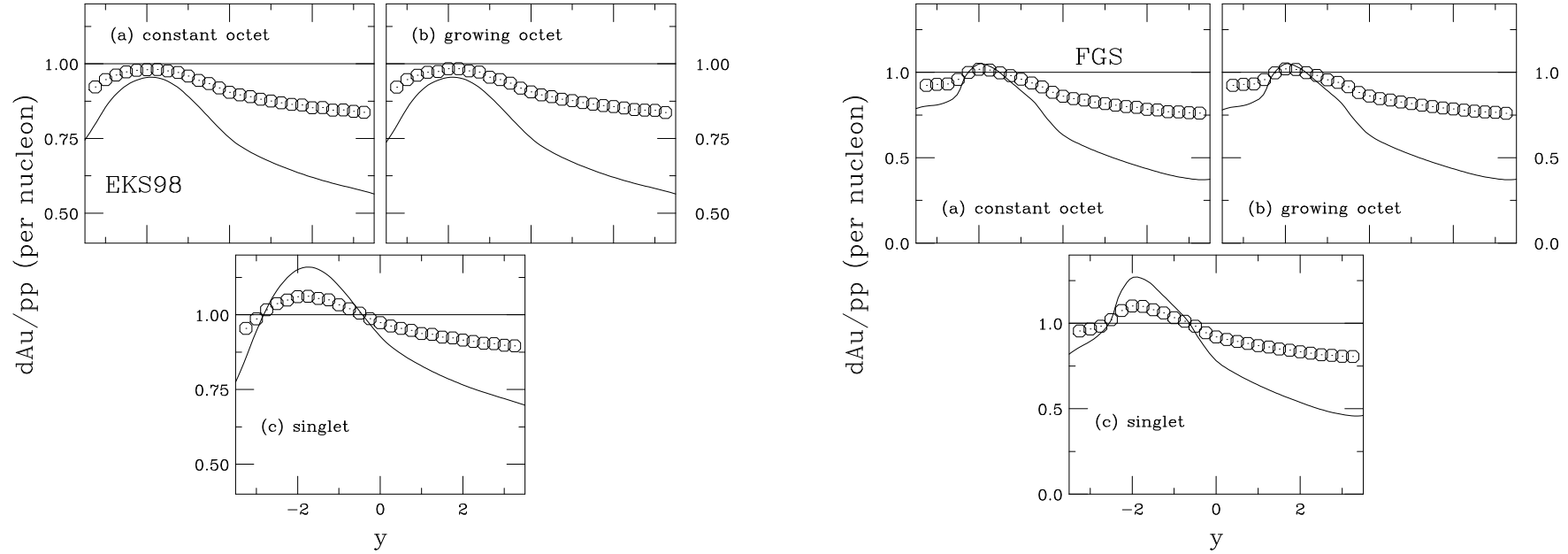# Inhomogeneous Shadowing and Absorption at RHIC

$$1.4 < b/R_A < 1.6$$

Figure 43: The J/ψ dAu/pp ratio at 200 GeV with EKS98 (left) and FGS (right) shadowing as a function of rapidity for (a) constant octet (assuming all states have a constant cross section and do not hadronize in the nucleus), (b) growing octet (states behave as singlets if they materialize in the medium), (c) singlet, all calculated in the CEM. The solid curves are the homogenous results while the points are impact parameter dependent shadowing, proportional to the path length, and absorption.

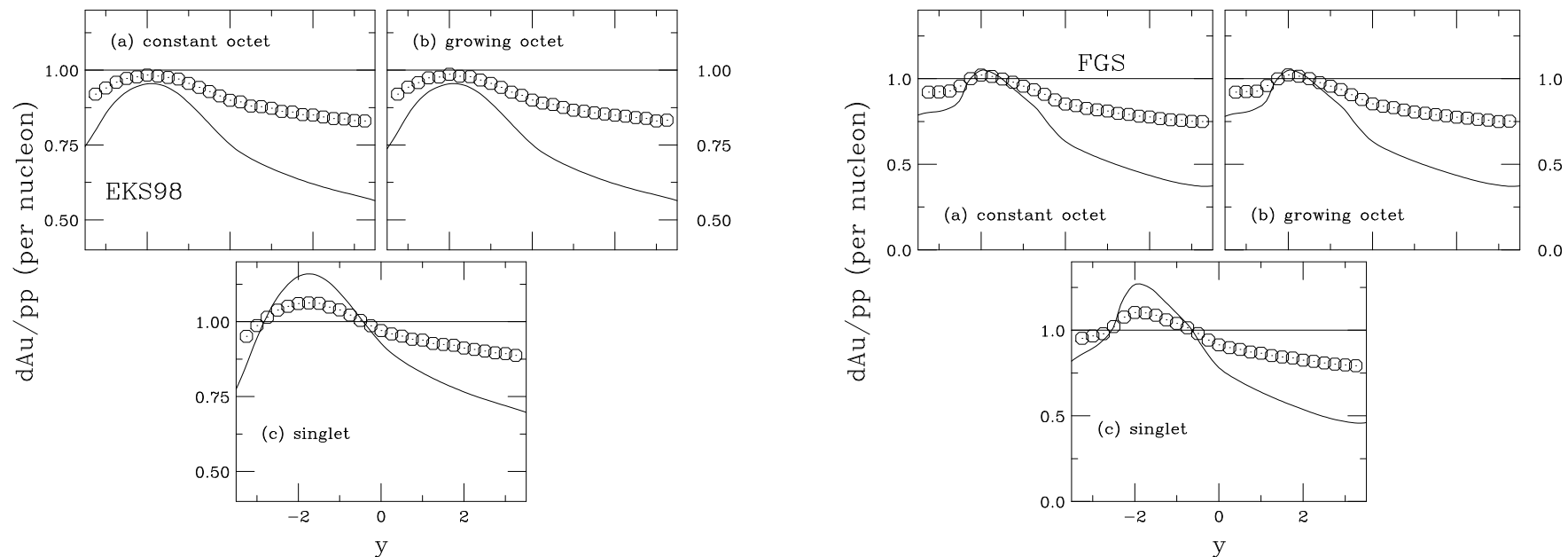# Inhomogeneous Shadowing and Absorption at RHIC

$$1.6 < b/R_A < 1.8$$

Figure 44: The J/ψ dAu/pp ratio at 200 GeV with EKS98 (left) and FGS (right) shadowing as a function of rapidity for (a) constant octet (assuming all states have a constant cross section and do not hadronize in the nucleus), (b) growing octet (states behave as singlets if they materialize in the medium), (c) singlet, all calculated in the CEM. The solid curves are the homogenous results while the points are impact parameter dependent shadowing, proportional to the path length, and absorption.

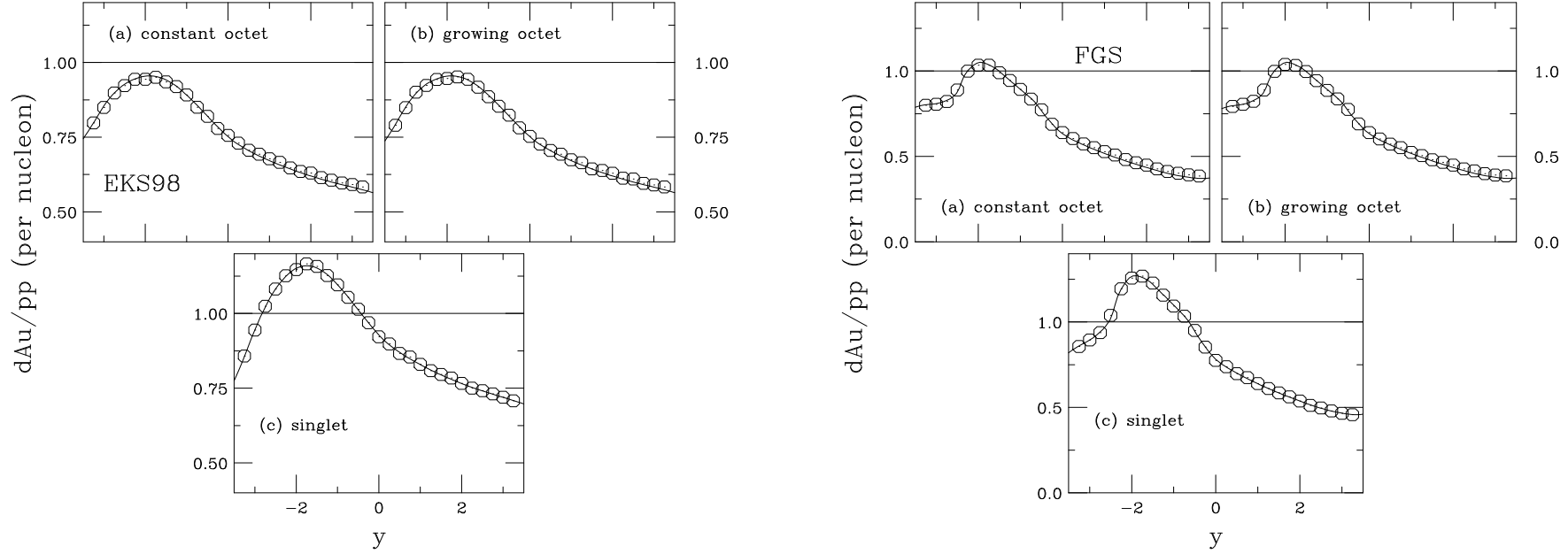# Inhomogeneous Shadowing and Absorption at RHIC

$$1.8 < b/R_A < 2.0$$

Figure 45: The J/ψ dAu/pp ratio at 200 GeV with EKS98 (left) and FGS (right) shadowing as a function of rapidity for (a) constant octet (assuming all states have a constant cross section and do not hadronize in the nucleus), (b) growing octet (states behave as singlets if they materialize in the medium), (c) singlet, all calculated in the CEM. The solid curves are the homogenous results while the points are impact parameter dependent shadowing, proportional to the path length, and absorption.

Inhomogeneous Shadowing and Absorption at RHIC

$$2.0 < b/R_A < 2.2$$

Figure 46: The J/ψ dAu/pp ratio at 200 GeV with EKS98 (left) and FGS (right) shadowing as a function of rapidity for (a) constant octet (assuming all states have a constant cross section and do not hadronize in the nucleus), (b) growing octet (states behave as singlets if they materialize in the medium), (c) singlet, all calculated in the CEM. The solid curves are the homogenous results while the points are impact parameter dependent shadowing, proportional to the path length, and absorption.

Inhomogeneous Shadowing and Absorption at RHIC

$$0 < b < 20 \text{ fm}$$


Figure 47: The J/ψ dAu/pp ratio at 200 GeV with EKS98 (left) and FGS (right) shadowing as a function of rapidity for (a) constant octet (assuming all states have a constant cross section and do not hadronize in the nucleus), (b) growing octet (states behave as singlets if they materialize in the medium), (c) singlet, all calculated in the CEM. The solid curves are the homogenous results while the points are impact parameter dependent shadowing, proportional to the path length, and absorption.

Inhomogeneous Shadowing and Absorption at the LHC
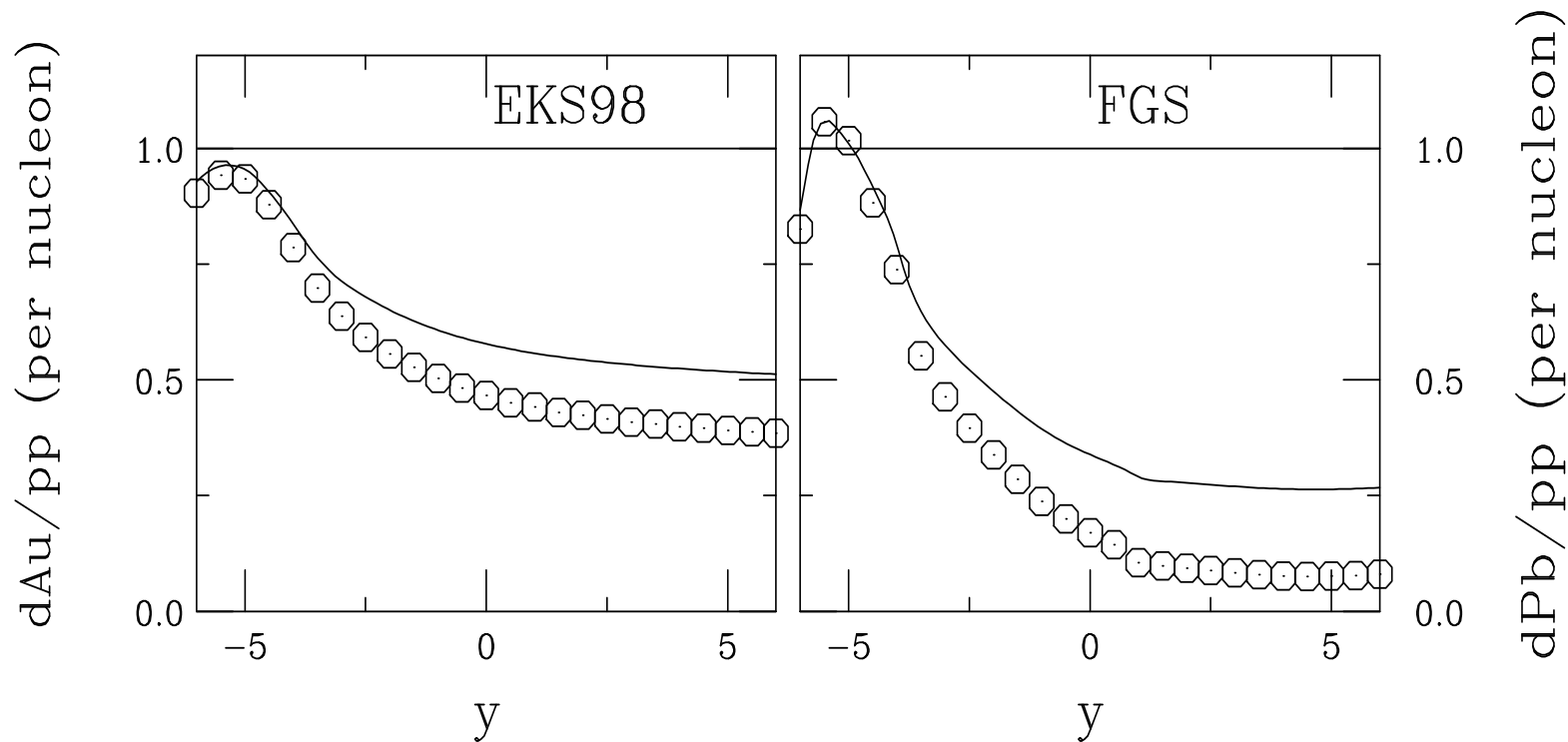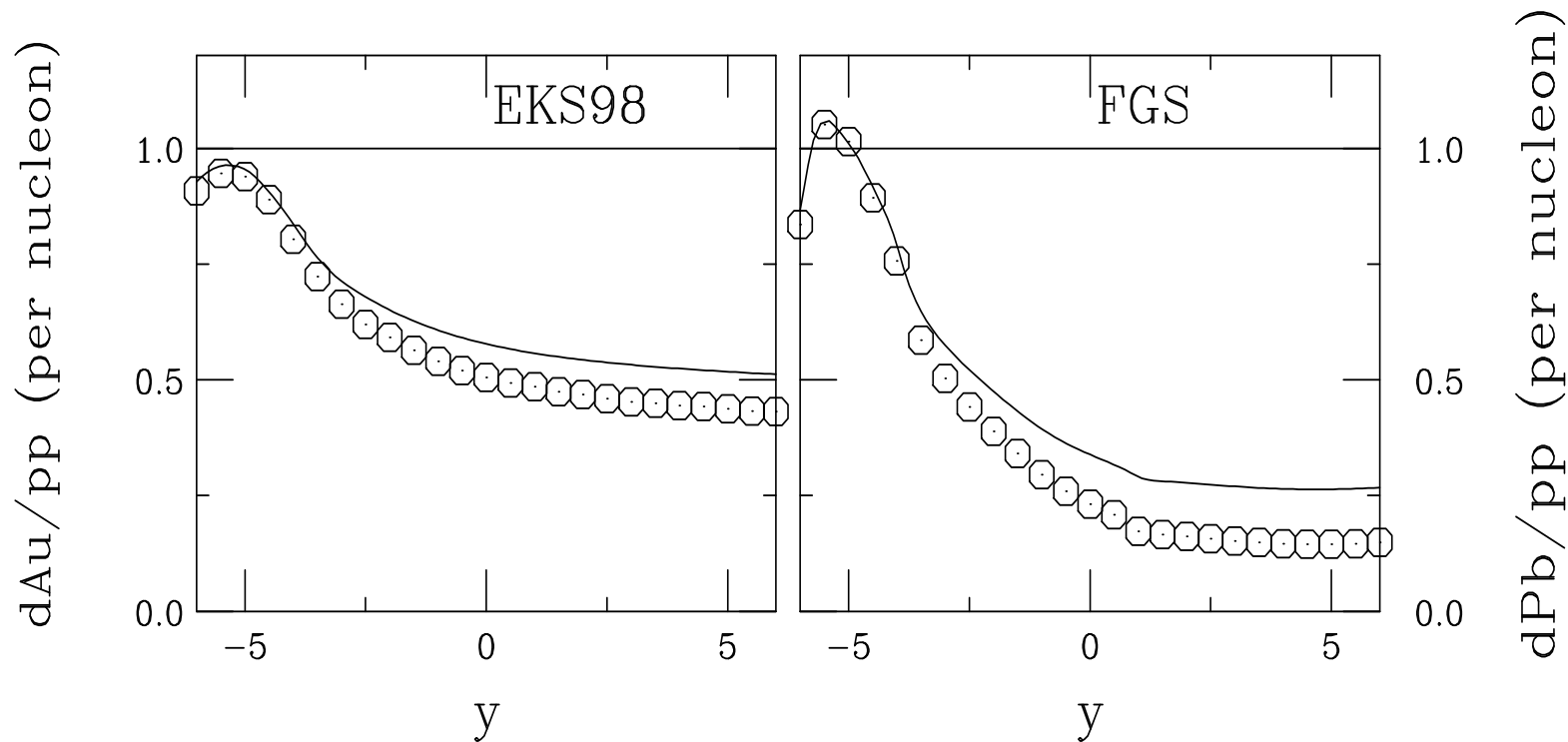
$$0 < b/R_A < 0.2$$
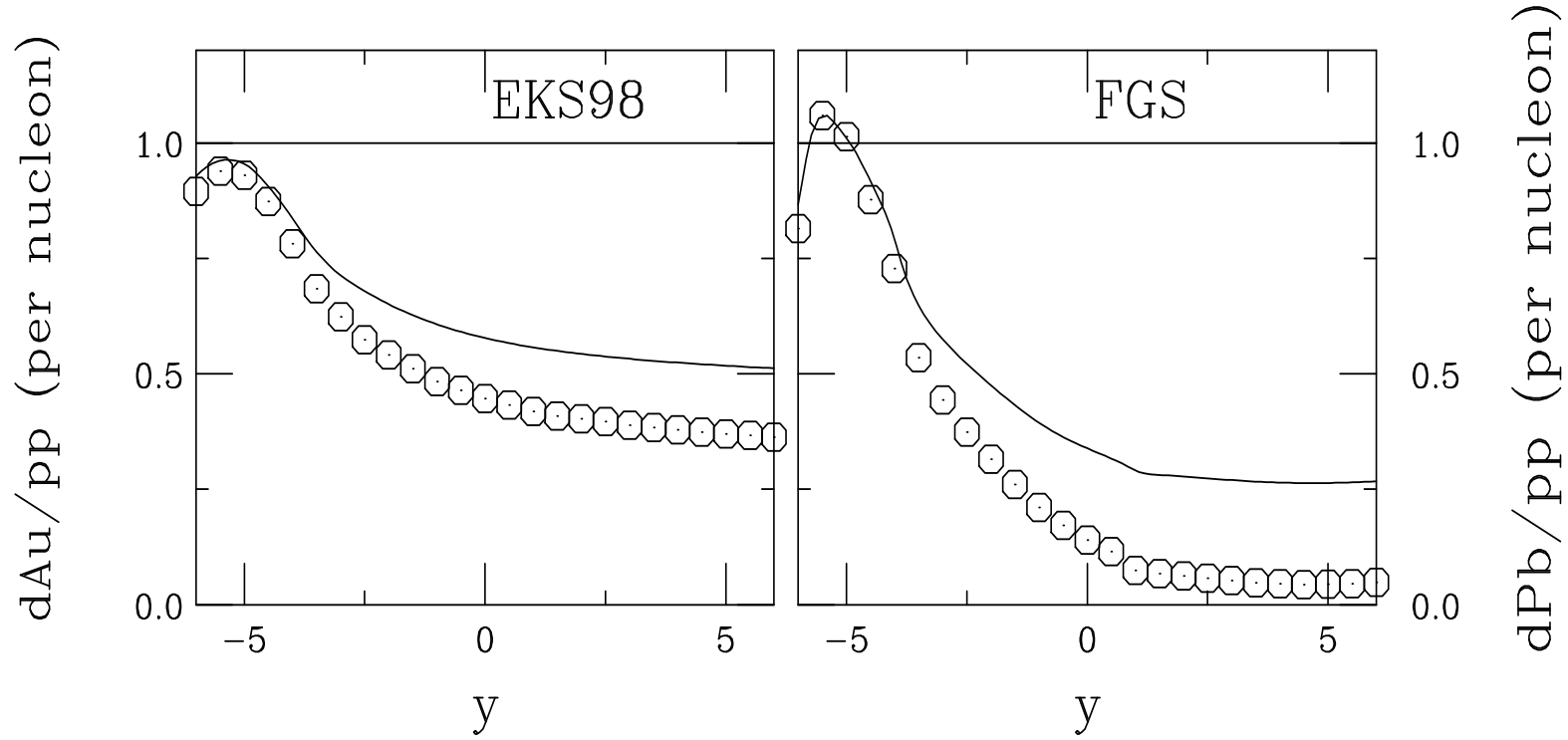
Figure 48: The J/ψ dPb/pp ratio at 6.2 TeV with EKS98 (left) and FGS (right) shadowing as a function of rapidity for the growing octet cross section, calculated in the CEM. The solid curves are the homogenous results while the points are impact parameter dependent shadowing, proportional to the path length, and absorption.

Inhomogeneous Shadowing and Absorption at the LHC

$$0.2 < b/R_A < 0.4$$

Figure 49: The J/ψ dPb/pp ratio at 6.2 TeV with EKS98 (left) and FGS (right) shadowing as a function of rapidity for the growing octet cross section, calculated in the CEM. The solid curves are the homogenous results while the points are impact parameter dependent shadowing, proportional to the path length, and absorption.

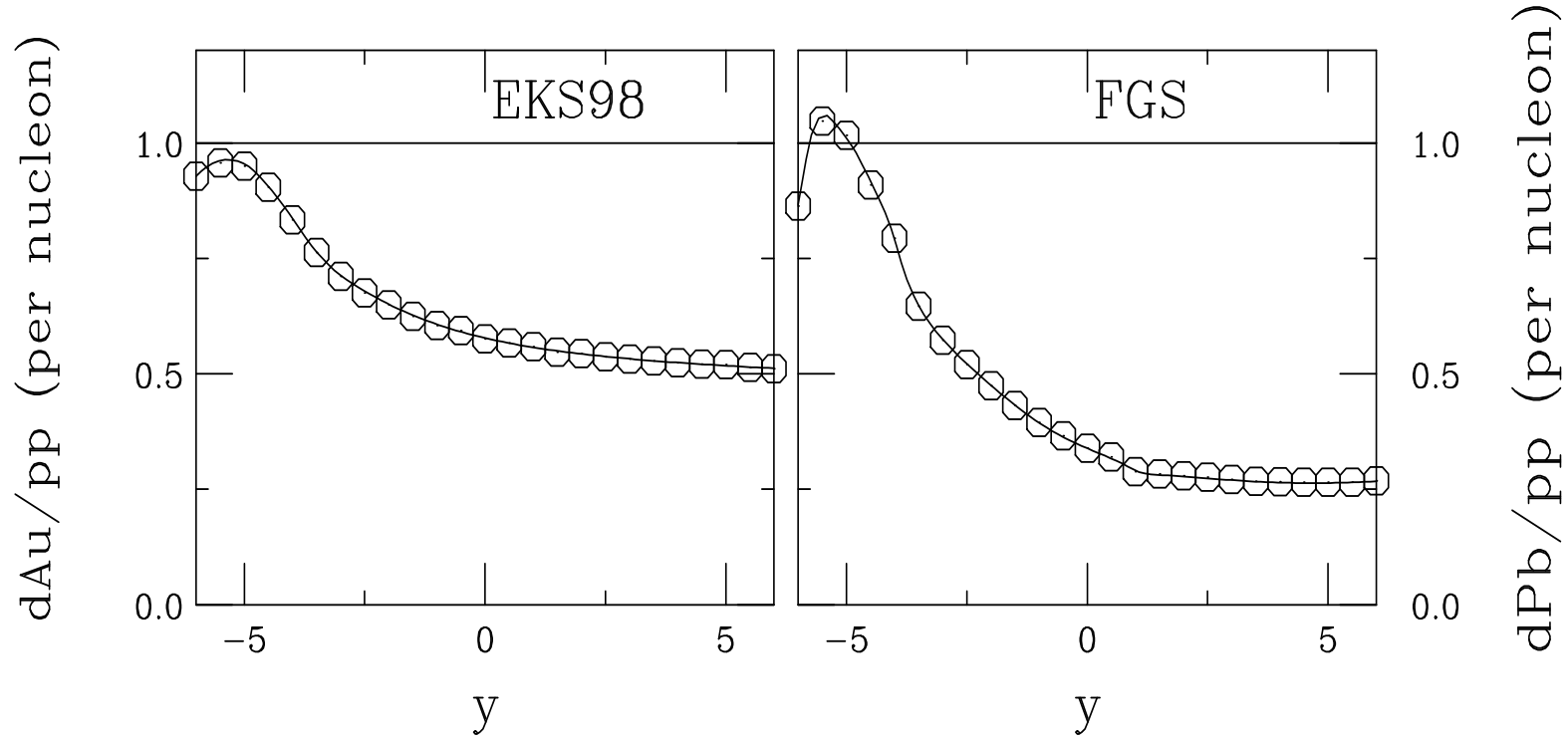# Inhomogeneous Shadowing and Absorption at the LHC

$$0.4 < b/R_A < 0.6$$

Figure 50: The J/ψ dPb/pp ratio at 6.2 TeV with EKS98 (left) and FGS (right) shadowing as a function of rapidity for the growing octet cross section, calculated in the CEM. The solid curves are the homogenous results while the points are impact parameter dependent shadowing, proportional to the path length, and absorption.

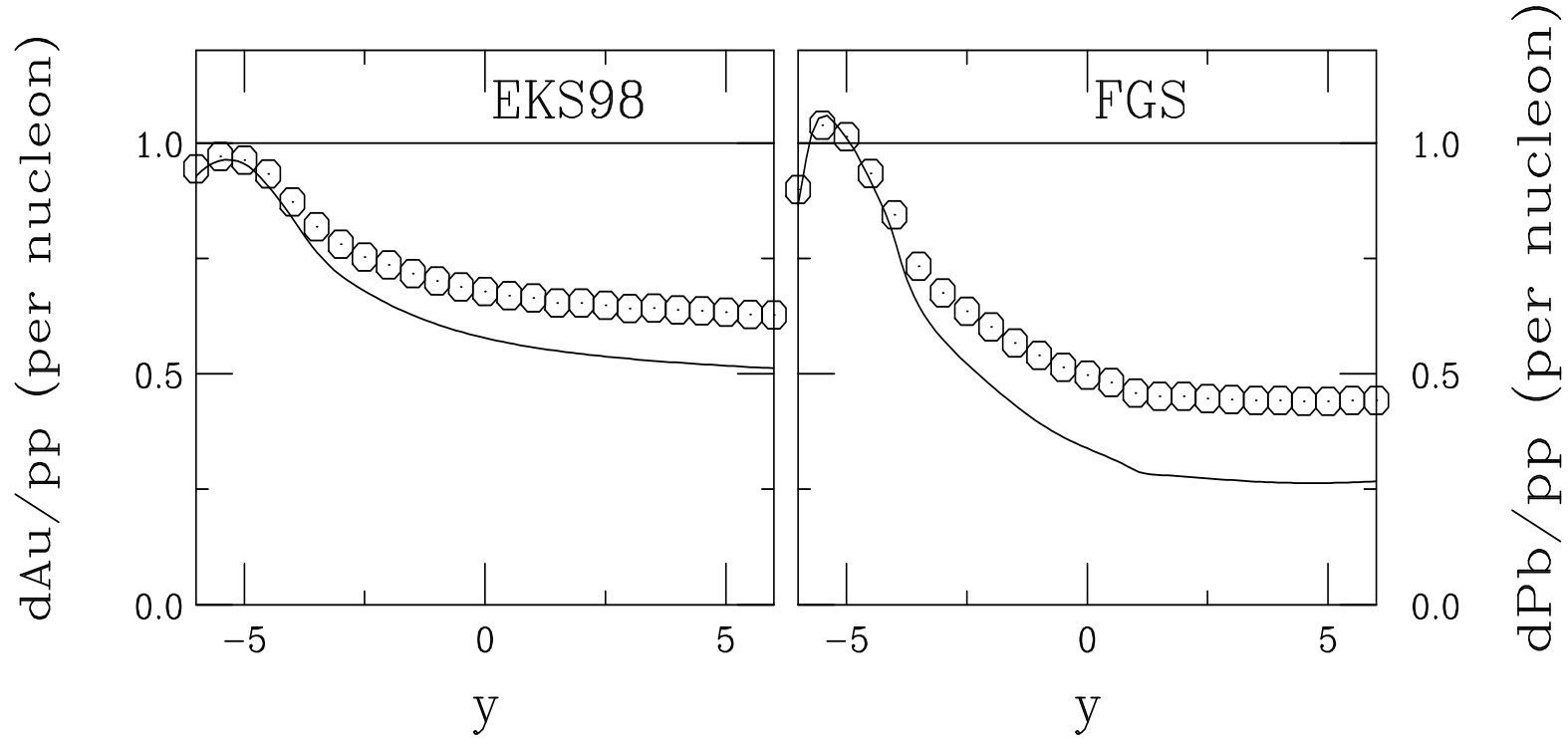# Inhomogeneous Shadowing and Absorption at the LHC

$$0.6 < b/R_A < 0.8$$

Figure 51: The J/ψ dPb/pp ratio at 6.2 TeV with EKS98 (left) and FGS (right) shadowing as a function of rapidity for the growing octet cross section, calculated in the CEM. The solid curves are the homogenous results while the points are impact parameter dependent shadowing, proportional to the path length, and absorption.

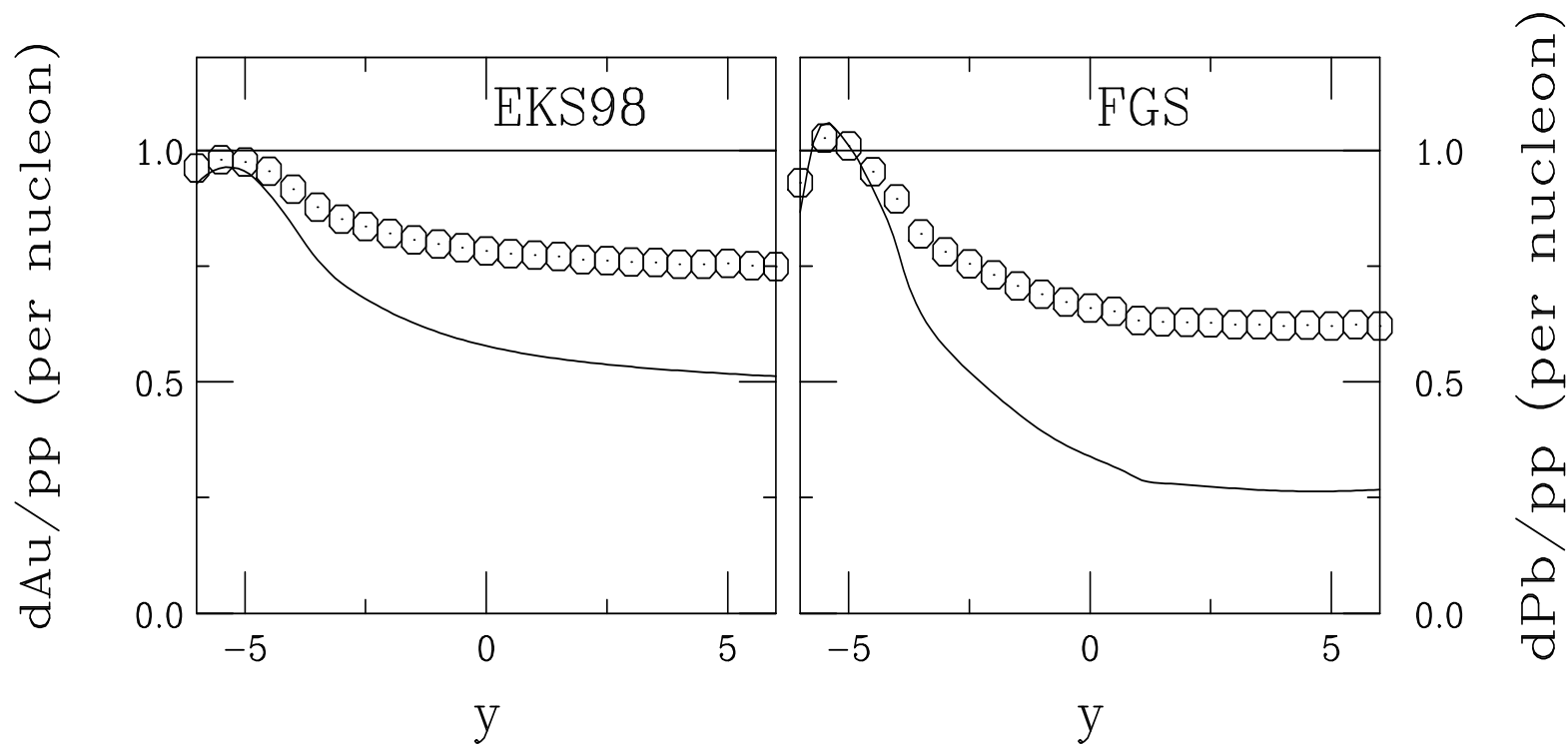# Inhomogeneous Shadowing and Absorption at the LHC

$$0.8 < b/R_A < 1.0$$

Figure 52: The J/ψ dPb/pp ratio at 6.2 TeV with EKS98 (left) and FGS (right) shadowing as a function of rapidity for the growing octet cross section, calculated in the CEM. The solid curves are the homogenous results while the points are impact parameter dependent shadowing, proportional to the path length, and absorption.

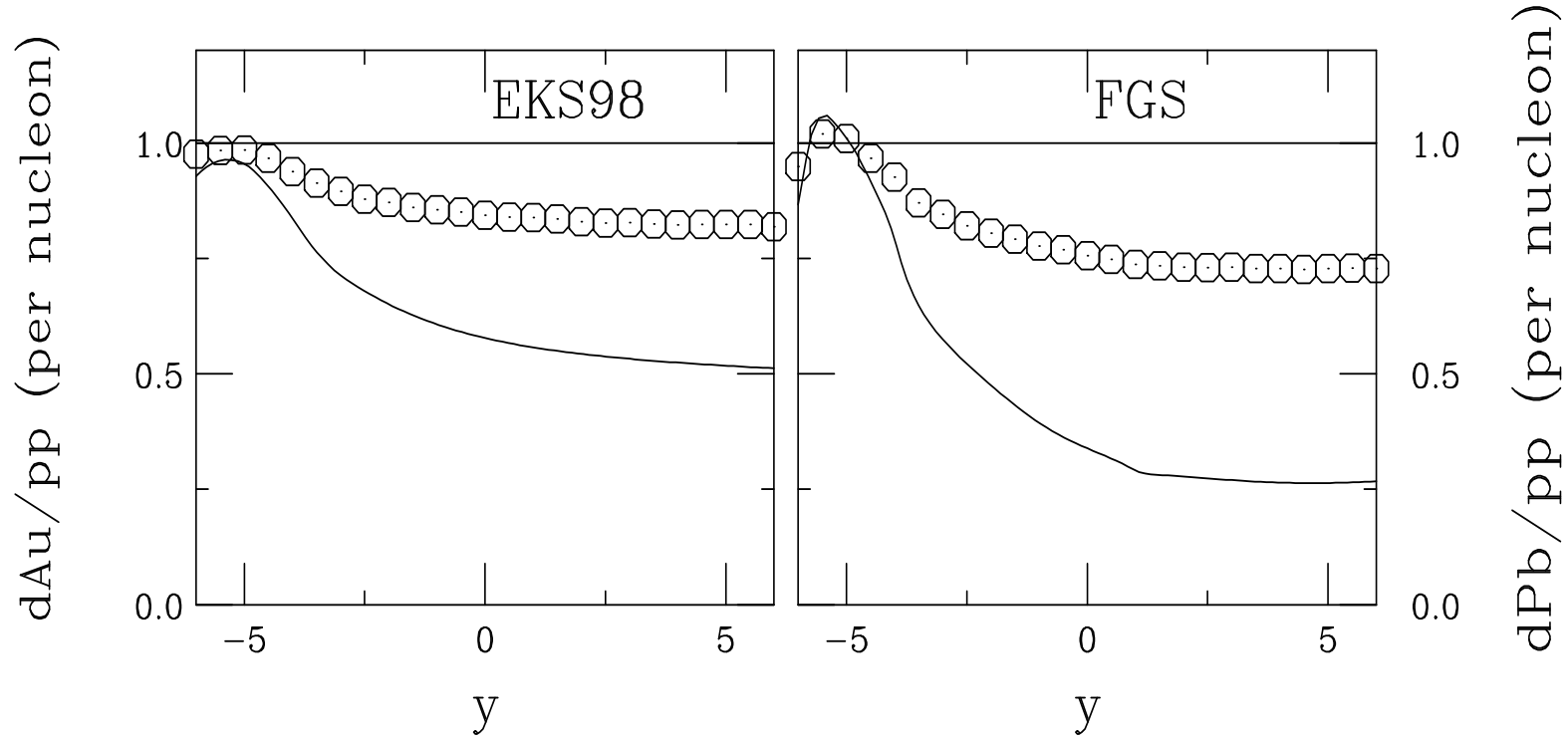# Inhomogeneous Shadowing and Absorption at the LHC

$$1.0 < b/R_A < 1.2$$

Figure 53: The J/ψ dPb/pp ratio at 6.2 TeV with EKS98 (left) and FGS (right) shadowing as a function of rapidity for the growing octet cross section, calculated in the CEM. The solid curves are the homogenous results while the points are impact parameter dependent shadowing, proportional to the path length, and absorption.

Inhomogeneous Shadowing and Absorption at the LHC

$$1.2 < b/R_A < 1.4$$

Figure 54: The J/ψ dPb/pp ratio at 6.2 TeV with EKS98 (left) and FGS (right) shadowing as a function of rapidity for the growing octet cross section, calculated in the CEM. The solid curves are the homogenous results while the points are impact parameter dependent shadowing, proportional to the path length, and absorption.

Inhomogeneous Shadowing and Absorption at the LHC
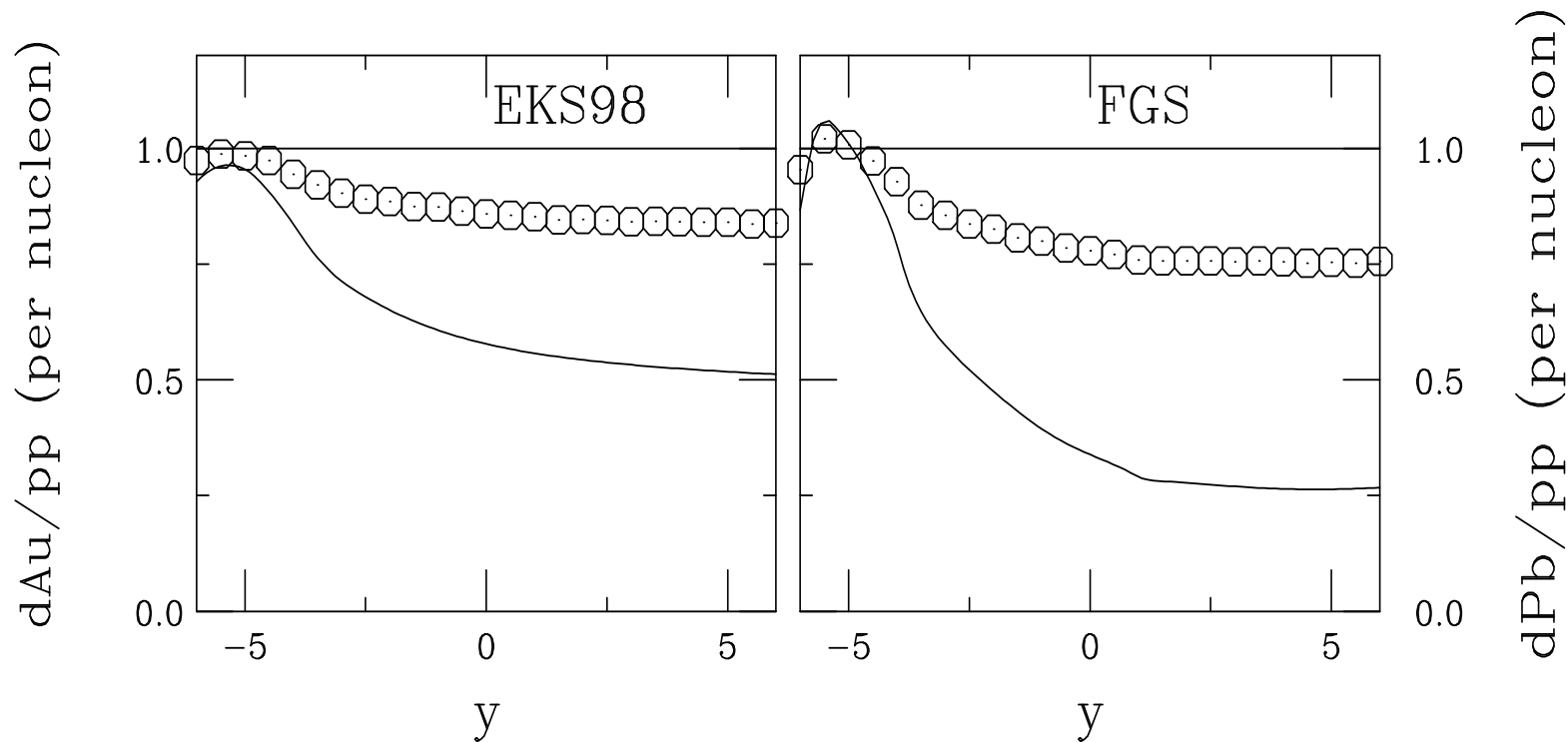
$$1.4 < b/R_A < 1.6$$

Figure 55: The J/ψ dPb/pp ratio at 6.2 TeV with EKS98 (left) and FGS (right) shadowing as a function of rapidity for the growing octet cross section, calculated in the CEM. The solid curves are the homogenous results while the points are impact parameter dependent shadowing, proportional to the path length, and absorption.

Inhomogeneous Shadowing and Absorption at the LHC
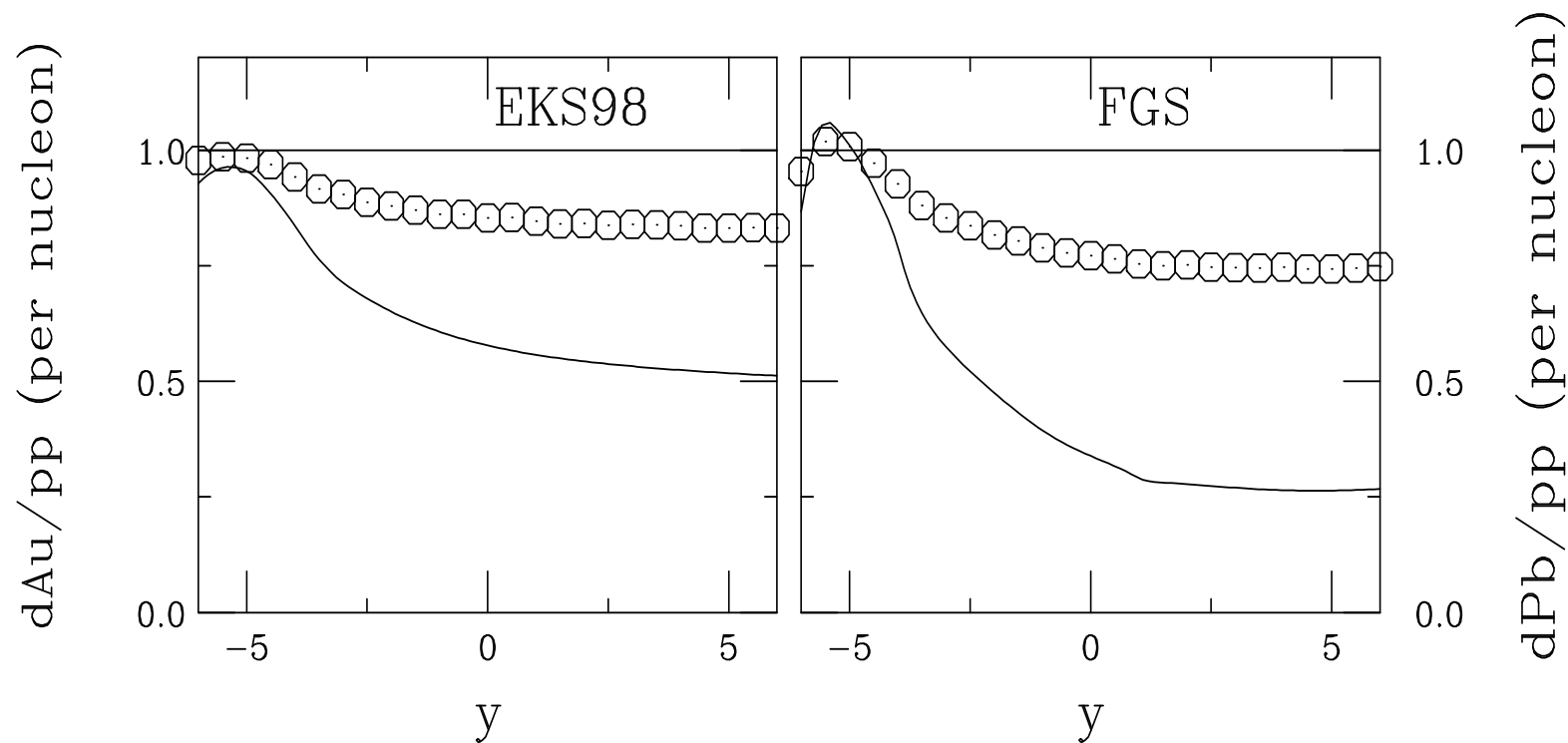
$$1.6 < b/R_A < 1.8$$

Figure 56: The J/ψ dPb/pp ratio at 6.2 TeV with EKS98 (left) and FGS (right) shadowing as a function of rapidity for the growing octet cross section, calculated in the CEM. The solid curves are the homogenous results while the points are impact parameter dependent shadowing, proportional to the path length, and absorption.

Inhomogeneous Shadowing and Absorption at the LHC
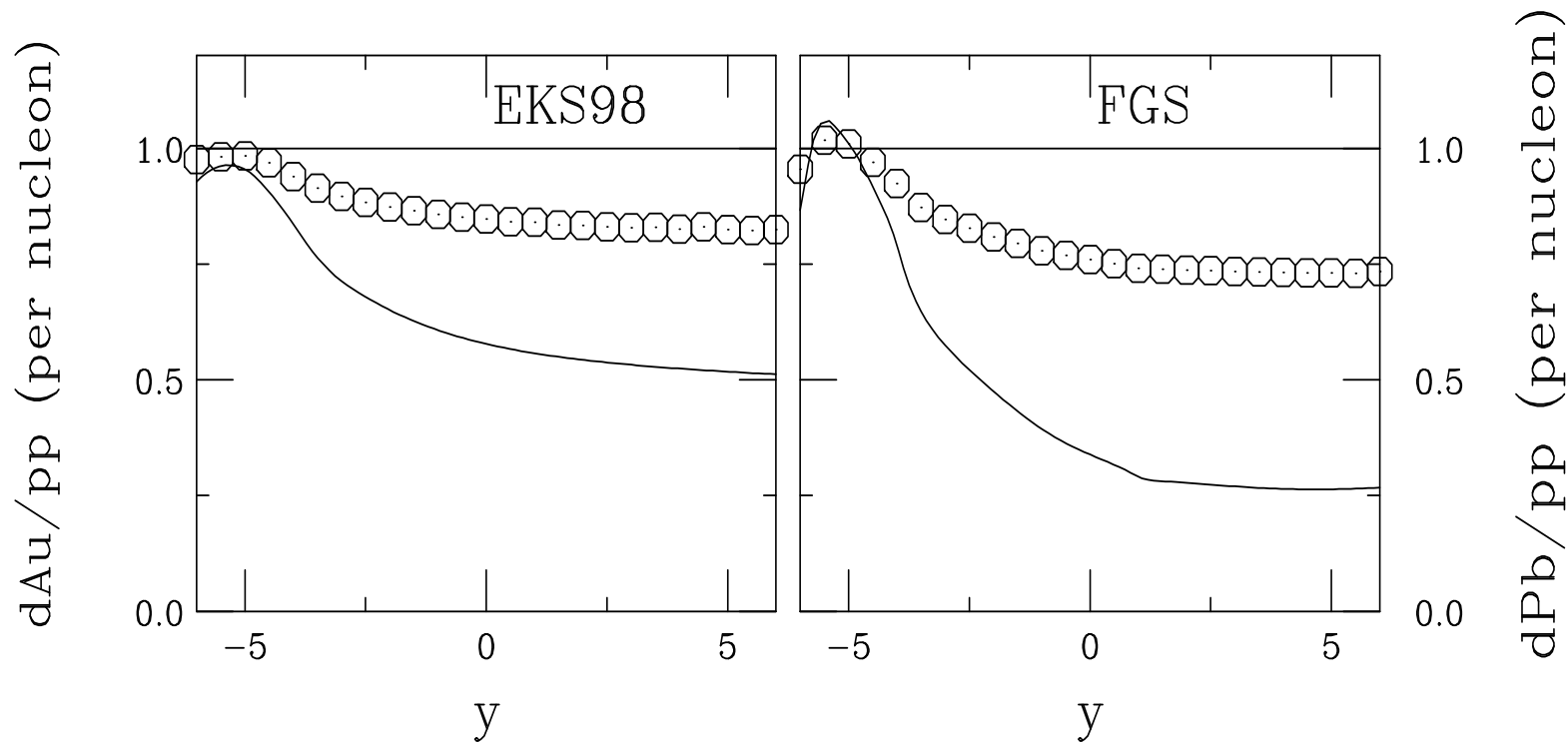
$$1.8 < b/R_A < 2.0$$

Figure 57: The J/ψ dPb/pp ratio at 6.2 TeV with EKS98 (left) and FGS (right) shadowing as a function of rapidity for the growing octet cross section, calculated in the CEM. The solid curves are the homogenous results while the points are impact parameter dependent shadowing, proportional to the path length, and absorption.

Inhomogeneous Shadowing and Absorption at the LHC
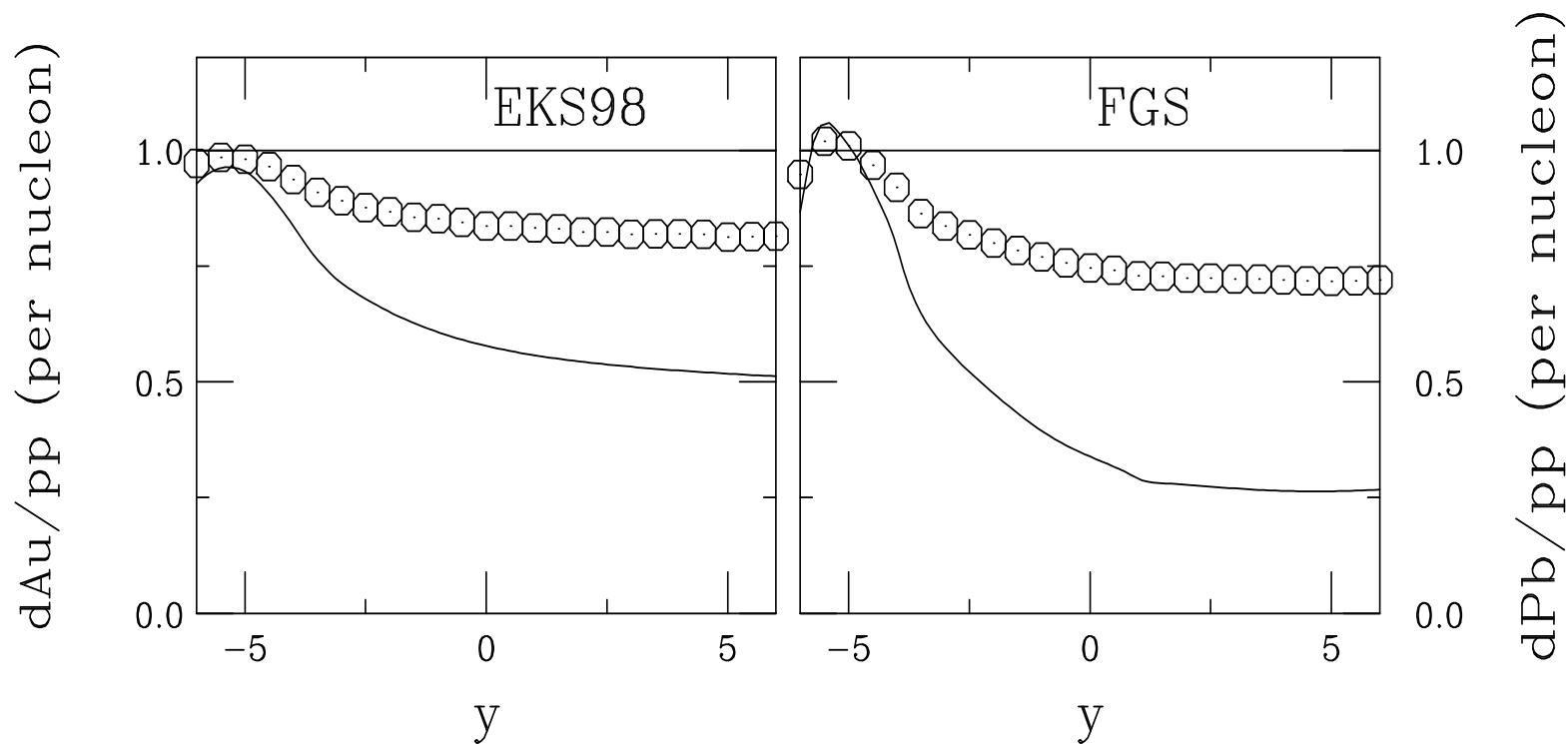
$$2.0 < b/R_A < 2.2$$

Figure 58: The J/ψ dPb/pp ratio at 6.2 TeV with EKS98 (left) and FGS (right) shadowing as a function of rapidity for the growing octet cross section, calculated in the CEM. The solid curves are the homogenous results while the points are impact parameter dependent shadowing, proportional to the path length, and absorption.

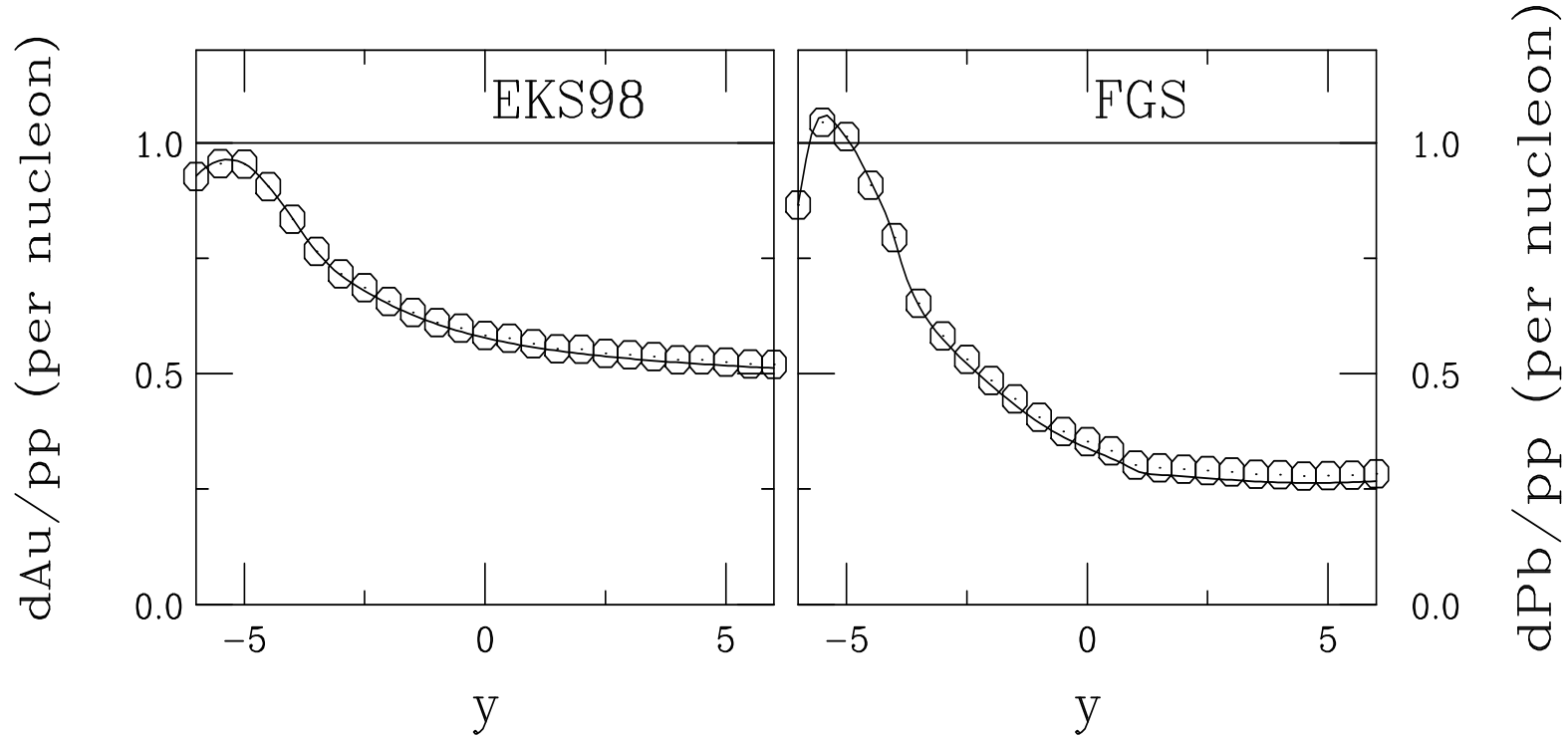# Inhomogeneous Shadowing and Absorption at the LHC

$$0 < b < 20 \text{ fm}$$

Figure 59: The J/ψ dPb/pp ratio at 6.2 TeV with EKS98 (left) and FGS (right) shadowing as a function of rapidity for the growing octet cross section, calculated in the CEM. The solid curves are the homogenous results while the points are impact parameter dependent shadowing, proportional to the path length, and absorption.

Summary

Lots of things we don't understand yet

Why is the STAR $c\bar{c}$ cross section so big relative to other measurements?

Does fragmentation really factorize?

What is the relative importance of shadowing and absorption in J/ψ production?

How important is regeneration of J/ψ in AA?

How well can we extrapolate to higher energies?

More data will help complete this picture